INVESTIGATION OF MECHANICAL TWINNING VIA MEASUREMENTS OF TEMPERATURE AND STRAIN FIELDS

by

Sefer Can Erman

B.S., Manufacturing Engineering, İstanbul Technical University, 2020

Submitted to the Institute for Graduate Studies in
Science and Engineering in partial fulfillment of
the requirements for the degree of
Master of Science

Graduate Program in Mechanical Engineering
Boğaziçi University

2023

ACKNOWLEDGEMENTS

I would like to thank my parents for their encouragement. My dad, Ahmet Erman, had always supported me unconditionally when I focused on my education. My mom, Dilek Erman, has dedicated her life to me without any expectations. I am deeply grateful to her for accompanying me and making me who I am. My brother, Çağatay Erman, has always stood by without any hesitation.

I would like to express my gratitude to my thesis supervisor Assoc. Prof. C. Can Aydıner for his guidance and support during my master's study. I would like to thank my thesis committee, Prof. Hasan Bedir, and Assist Prof. Alpay Oral for their remarks.

I am deeply grateful to my lab partner in the Mechanics of Advanced Material Laboratory, Necdet Ali Özdür. Also, I appreciate Rian Seghir from Ecole Centrale Nantes's invaluable contribution to my thesis. I want to thank my dear friend Nezir Özdemir who has been with me since my undergraduate years. I would like to thank my dear friend Uğur Özküsen who accompanied me during my master's journey and supported me against all kinds of difficulties.

This work was supported by the Scientific and Technological Research Council of Turkey (TÜBİTAK), Grant No: 120N722.

ABSTRACT

INVESTIGATION OF MECHANICAL TWINNING VIA MEASUREMENTS OF TEMPERATURE AND STRAIN FIELDS

Wrought magnesium exhibits deformation complexity with high load path dependency and plastic anisotropy. Lightweight magnesium AZ31 is widely used in literature for twinning investigations due to the ease of $\{10\bar{1}2\}(\bar{1}011)$ tensile twin activation under favorable loading conditions. Coordinated propagation of twinning leads to strain localization across the aggregate in the form of macroscopic shear bands. When the load is reversed after twin growth, material undergoes detwinning that is crystallographic orientation transformation of twinned grains to the original position. The contributions of this thesis built on the previous OM-DIC studies are composed of two independent channels. First, a notched sample design is used to guide conjugate shear bands into predetermined diagonal corridors and enforce their overlap at a prefixed location to study the physics of the overlap with OM-DIC. Secondly, the energetic aspects of material deformation with emphasis on twinning and detwinning have been studied by in situ infrared thermography. The primary goal of this part is to reveal the stored energy in the material over cyclic deformation that entails twinning/detwinning and slip plasticity regimes. Absolute temperature measurements with IRT conducted are successfully achieved by attaching an undeformed (free hanging) reference material next to the actual sample and the temperature data considered is the differential between deformed and undeformed material. Further, the reference material is also thermally insulated from the sample during by inserting a thermal isolator for more robust results. In the big picture, these experimental results will help the validation of higher fidelity crystal plasticity models for magnesium.

ÖZET

MEKANİK İKİZLENMENİN GERİNİM ALANLARI VE SICAKLIK ÖLÇÜMLERİYLE İNCELENMESİ

İşlenmiş magnezyum metalinin deformasyonu bazı sebeplerden dolayı karmaşıktır. Bu karmaşıklık magnezyumun fiziksel özelliklerinin ve yüklemenin yöne bağımlılığından kaynaklanır. Hafif bir metal olan magnezyum literatürde ikizlenme olayının incelenmesinde sıkça kullanılır. Çünkü $\{10\bar{1}2\}(\bar{1}011)$ çekme ikizlenmesi magnezyumda kolayca aktive edilebilir. Koordine ikizlenme hareketi magnezyumda makroskobik ölçüde kayma bantlarına sebep olur. Eğer yükleme yönü tersine çevrilirse, ikizlenmenin görüldüğü taneler ikizlenme tersinimi ile kendi kristalografik yönelimlerini orijinal pozisyonlarına değiştirirler. Bu tezin katkıları daha önceki optik mikroskopla (OM) yapılan dijital imge korelasyonu (DIC) çalışmalarına nazaran iki ayrı kanal içermesidir. İlk olarak, çentikli numune konjuge kayma bantlarını önceden belirlenmiş bir koridor üzerinde yönlendirmek ve önceden belirlenmiş bir lokasyonda çakıştırmak için tasarlanmıştır. Bu sayede çakışan bantların fiziği OM-DIC ile incelenecektir. İkinci olarak, ikizlenme ve ikizlenme tersinimi deformasyon mekanizmaları enerji açısından kızılötesi termografi ile çalışılmıştır. Buradaki asıl amaç, periyodik yükleme (ikizlenmeyi ve ikizlenme tersinimini incelemeye imkân sağlar) ile malzemede depolanan enerjiyi açığa çıkarmaktır. Mutlak sıcaklık ölçümleri deney numunesinin yanına deforme olmayacak bir malzeme iliştirilerek başarılmıştır. Mutlak sıcaklık ölçümleri deney numunesinden referans malzemesinin sıcaklığı çıkarılarak hesaplanmıştır. Ayrıca, deney numunesi ile referans malzemesi arasına ısıl yalıtkan bir malzeme eklenerek deney numunesi termal açıdan izole edilmiştir. Bu çalışmanın bütününe bakacak olursak, buradan elde edilen deneysel sonuçlar magnezyum için daha yüksek doğruluk içeren kristal plastisite modellerinin doğrulanmasına yardımcı olacaktır.

TABLE OF CONTENTS

ACKNOWLEDGEMENTS . . . iii
ABSTRACT . . . iv
ÖZET . . . v
LIST OF FIGURES . . . viii
LIST OF TABLES . . . xii
LIST OF SYMBOLS . . . xiii
LIST OF ACRONYMS/ABBREVIATIONS . . . xiv
1. INTRODUCTION . . . 1
1.1. Motivation . . . 1
1.2. Scope and Objectives . . . 3
2. BACKGROUND . . . 6
2.1. Magnesium Deformation Mechanics with Twinning and Detwinning . . . 6
2.2. Experimental Investigation of Twin Driven Deformation . . . 9
2.3. Infrared Thermography in Mechanics . . . 11
2.4. On banded structures with IRT measurement . . . 12
2.5. Infrared Thermography Uniaxial Testing . . . 13
3. MATERIALS & METHODS . . . 17
3.1. Sample Specifications . . . 17
3.2. Material Texture . . . 19
3.3. Sample Preparation . . . 20
3.3.1. Sample preparation for micro-DIC . . . 20
3.3.1.1. Hot Mounting . . . 21
3.3.1.2. Grinding . . . 22
3.3.1.3. Polishing . . . 22
3.3.1.4. Etching . . . 22
3.3.1.5. DIC speckle pattern . . . 22
3.3.2. Sample preparation for IRT . . . 23
3.4. Experimental Setup . . . 24

3.5. Data Collection and Analysis 28
3.5.1. Multi-scale DIC over the notched sample 28
3.5.2. IRT 30
3.5.3. IRT-DIC 31
4. RESULTS 33
4.1. In situ micro-DIC experiments on the cross-notched geometry 33
4.2. In situ infrared thermography over cyclic loading 36
4.2.1. Cycle 1 Compression 40
4.2.2. Cycle 1 Tension 44
4.2.3. Stored energy during cyclic loading 45
5. DISCUSSION 52
6. CONCLUSION 55
7. FUTURE WORK 57
REFERENCES 58

LIST OF FIGURES

Figure 2.1. Twin and slip mechanism for magnesium over unit cell. 6

Figure 2.2. Consequtive deformation of parallel planes that undergo twinning due to shearing. 7

Figure 2.3. Asymmetric stress strain curve of cyclic loading of rolled Mg AZ31. 9

Figure 2.4. x-y coordinate system on the dog-bone sample. 14

Figure 3.1. Representation of sample geometries. 17

Figure 3.2. Representation of sample geometries. 18

Figure 3.3. Representation hot rolled plate and the hexagonal unit cell with coordinates: rolling direction, transverse direction, normal direction is denoted as RD, TD, ND. 19

Figure 3.4. (a) 0002 pole figure for rolled material, (b) 0002 pole figure for extruded material, (c) $10\bar{1}0$ pole figure for extruded material. . . . 20

Figure 3.5. Cross-notched sample in a bakelite mold. 21

Figure 3.6. (a) a single micro frame, (b) same neighborhood with (a) with speckle addition. 23

Figure 3.7. Specimen configuration for thermal measurements 24

Figure 3.8. Multi-scale deformation measurement setup at the Mechanics of Advanced Materials Laboratory with elements (a) tension-compression module (b) macro-DIC line, (c) micro-DIC line, (d) IRT camera, (e) x-y-z positioners, (f) load display unit, (g) load controller, (h) macro-DIC light, (i) micro-DIC light, (j) vibration isolated optical table, (k) opaque curtain. 25

Figure 3.9. Macro-DIC image of the specimen which contains micro-DIC scan grid. 27

Figure 3.10. (a) a single micrograph (b) a smaller granular neighborhood (blue box in (a)) with the utilized DIC grid overlaid with red dots, (c) a speckled grain field (black box in (a)) from undeformed the scanned region. 29

Figure 3.11. Visualization of thermal recording frame with various boxes that represent temperature field of the specimen and reference part. . . 30

Figure 3.12. A single thermal camera frame that is used to measure strain with DIC subset. 31

Figure 3.13. Optical microscopy image for macro-DIC. 32

Figure 4.1. (a)-(k) Full-field (stitched) micro-DIC axial strain, (ε_{yy}), maps at load points (a-k) indicated over (l), the engineering stress versus average strain curve of the sample under compression; (m) macro-DIC (ε_{yy}) map at point i for comparison. 34

Figure 4.2. (a) - (c) Axial strain maps, (d) engineering stress-axial macro strain curve of the transversely isotropic extruded sample under compression, (e) axial strain contours (at 1.5% absolute average strain) on the surface of a 3D finite element analysis (actual analysis domain on the left) that considers isotropic Mises plasticity. 35

Figure 4.3. Stress-strain curve of the cyclic experiment over rolled magnesium AZ31. 37

Figure 4.4. (a) Reference (top rectangle) and deformed (bottom rectangle) ROIs on a representative thermal image at the beginning of the experiment (b) Overall temperature profile in compression. 40

Figure 4.5. Combine stress and temperature difference curve over axial strain. 41

Figure 4.6. τ_{eq} calculation after cycle 1 compression. 42

Figure 4.7. Overall temperature profile in cycle 1 tension. 43

Figure 4.8. Temperature and force measurements over strain. 44

Figure 4.9. Energy terms for cycle 1 compression. 46

Figure 4.10. Energy terms for cycle 1 tension. 47

Figure 4.11. Energy terms for cycle 4 tension. 48

Figure 4.12. Overall temperature profile in cycle 4 tension. 49

Figure 4.13. Taylor-Quinney coefficient variation during (a) cycle 1 compression (b) cycle 1 tension; red lines correspond to averages. 50

Figure 5.1. Reference (bottom rectangle) and deformed (top rectangle) ROIs on a representative thermal image for titanium specimen. 52

Figure 5.2. Temperature profile comparison between magnesium and titanium both in compression and tension. 53

LIST OF TABLES

Table 4.1. Experiment details of cyclic experiment. 38

Table 4.2. Axial micro strain averages after each loading of cyclic experiment (macro-DIC results). 39

LIST OF SYMBOLS

a, c	Lattice parameters of HCP unit cell
A_k	Set of thermodynamic forces
c_p	Specific heat capacity
k	Thermal conductivity coefficient
q	Heat flux
$\dot{Q}^e$	Heat generation during elastic deformation
$\dot{Q}^p$	Heat generation during plastic deformation
q	Heat flux
r	External heat supply
T	Temperature
V_k	Set of internal variables
W_p	Total plastic work
α	Thermal expansion coefficient
β	Taylor-Quinney coefficient
ε	Infinitesimal strain
ε_{yy}	Axial micro-DIC strain
$\underline{\underline{\varepsilon}}^e$	Elastic strain tensor
$\underline{\underline{\varepsilon}}^p$	Plastic strain tensor
λ, μ	Elastic constants
ρ	Density
σ	Stress
$\underline{\underline{\sigma}}$	Cauchy stress tensor
ψ	Helmholtz free energy
ω	Infinitesimal rotation

LIST OF ACRONYMS/ABBREVIATIONS

BCC	Body Centered Cubic
CRSS	Critical Resolved Shear Stress
DIC	Digital Image Correlation
ED	Extrusion Direction
EDM	Electrical Discharge Machining
FCC	Face Centered Cubic
FE	Finite Element
HCP	Hexagonal Close Packed
IR	Infrared
IRT	Infrared Thermography
IRT-DIC	Infrared Thermography Digital Image Correlation
LED	Light Emitting Diode
ND	Normal Direction
OM-DIC	Optical Microscopy Digital Image Correlation
RD	Rolling Direction
TD	Transverse Direction

1. INTRODUCTION

1.1. Motivation

Magnesium is a preferable structural metal owing to its high strength to density ratio. The combination of the strength and the lightweight of magnesium leads to a desirable material in several industries especially aerospace, automotive and electronics [1]. The plastic deformation of wrought magnesium, however, contains challenges. Both primary forms of wrought alloys (rolled and extruded) are imparted with very sharp crystallographic textures, and this makes the load path dependence and anisotropy of the material more pronounced [2] that is already adversely affected by the existence of multiple slip and twin systems that take part in the deformation of magnesium.

Magnesium formability is limited at room temperature (e.g., underlying the fact that the utilization of sheet-formed magnesium did not become widespread). The main reason for this poor formability is a limited number of slip systems in hexagonal closed packed (HCP) unit cell [2]. Characteristically, non-cubic materials have a limited number of primary slip systems and contain high-level plastic anisotropy [3]. The limited number of slip systems is compensated for by twinning in HCP metals.

Twinning is a deformation mechanism observed more commonly in low-symmetry metals, where the orientation of a band of material inside a crystallite is abruptly transformed to a mirror image with respect to a specific crystallographic plane (called the "twin plane") [4]. Like dislocation slip, mechanical twinning subjects a crystal to a permanent deformation with negligible amount volume difference. In contrast to dislocation slip, however, twinning imposes a characteristic amount of shear deformation in its locality ("transformation strain") [5]. Further, unlike dislocation slip, twin operation is unipolar, e.g., if a twin forms under compression, it does not form under tension. However, if a twin is formed in one sense of the load, if the load is reversed, the easiest way the material accommodates reverse strain becomes the reversal of the

twin domain, called "detwinning" [2]. Detwinning simply takes back the transformation strain.

Among hexagonal-close-packed metals with engineering utilization (titanium, zirconium, magnesium, etc.), magnesium, in particular, exhibits profuse twinning. It has thus become a model material for most twinning investigations aside from its technological importance. Both extruded and rolled magnesium under cyclic loading yields pronounced asymmetry in the form of sigmoidal stress-strain curves due to twinning (in one load sense) and detwinning (in the opposite load sense, operating at very low stress) [2]. Numerous recent studies investigate the twinning phenomena for magnesium both monotonic loading [6, 7] and cyclic loading [8] with a multitude of experimental and modelling techniques. Cyclic loading provides an opportunity to investigate detwinning in addition to twinning.

Another essential consequence of magnesium twinning in polycrystalline aggregates is the coordinated propagation of twinning that leads to strain localization at the component scale. Crudely, a mechanical twin that forms in one grain tends to instigate a twin in its neighbor and the repetition of this phenomenon leads to the continuous propagation of twins that is named autocatalytic twinning [9]. Consequently, autocatalytic twinning causes strain localization across the aggregate in the form of macroscopic shear bands. While these bands and their microstructural dependencies have been studied [10, 11] multi-face, multi-scale digital image correlation (DIC) measurements have only recently detailed the kinematics of these bands [12–14].

Fundamental-scale polycrystalline models have extreme difficulty in simulating the twin-based strain localization in magnesium deformation. In terms of the target length-scale, high-fidelity polycrystalline modeling efforts are in rough agreement with the aforementioned recent micro-DIC studies. Hence, they can be validated by these experiments in terms of the measured strain variable. Spatially resolved models that intend to capture local fields on realistic grain neighborhoods [15–18] have been gaining increasingly more ground. This approach is eyeing toward predicting material damage

and failure [17]. If universal crystal plasticity models can be conceived for magnesium, they can predict the plethora of different behavior this material exhibits for various crystallographic textures and load paths (e.g., [19]).

For verifying the universality of these models, it is important to pin them with different physical channels of measurement. A model that can meet strain fields (at some length-scale as determined by DIC) as well as temperature fields (under different types of deformation mode, e.g., twinning, detwinning, slip plasticity).

1.2. Scope and Objectives

This work is built on previous investigations of magnesium deformation conducted with an in house microscopic DIC setup that produced in-situ deformation fields of magnesium deformation. (The strain localization in unnotched Mg AZ31 sample was studied previously over profuse twinning [12], slip dominated [20], and cyclic load paths [13].) The primary component of this project is to add the capability to measure temperature fields incorporated to the aforementioned multi-scale DIC setup. The temperature measurement is conducted by infrared thermography (IRT) through a thermal camera that is appended to the in-house setup over its current optical, loading, and positional elements. In contrast to scanning microscopic DIC that has a sampling time in the order of minutes (and thus has no time resolution), IRT temperature field measurement can be conducted considerably faster (on the order of 100 Hz) around the twinning events. Temperature changes are utilized to reveal stored energy during cyclic deformation.

Using the newly constructed IRT channel, this work investigates the thermo-elastic and thermo-plastic behavior of magnesium AZ31 samples under cyclic load paths. Cyclic loading gives a chance to understand thermal behavior of different plastic deformation modes: twinning, detwinning, slip plasticity. During deformation, the proportion of plastic work which is converted to heat is represented with Taylor-Quinney coefficient (β) [21]. Classically, Taylor-Quinney coefficient is taken 0.9 in calculation [22], but

it undergoes large variation during loading in various material [23]. The literature for this field is too limited when magnesium is considered. Better thermo-mechanical characterization should be employed to fulfil need on the literature. This work promises a more complete physical description on plastic deformation of wrought magnesium, complementing the strain measurements to date. The outcome of this work will be used to better develop and calibrate crystal plasticity models.

In addition to thermal behavior of rolled and extruded Mg AZ31, there is a secondary and separate component to this thesis that uses the already established micro-DIC experimentation. Here, notched samples are considered with microscopic DIC—all previous experiments considered smooth/unnotched samples. A cross-notched sample is proposed to preordain the location of shear bands (it occurs randomly in unnotched sample) and to ensure overlap of the shear bands at exact location to study the physics of this interaction.

The original intention behind the use of notched samples was in fact related to the primary IRT measurement. The notches were placed to constrain the deformation spatially such that the concentration zone of the real-time IRT measurement could be known in advance. However, in reality, due to a combination of factors (high conductivity of magnesium, minimal scale of the sample dimension) we could not derive a spatial resolution out of the IRT measurements. However, very detailed micro-DIC strain field measurements, conducted in cross-notched samples, allowed us to better understand the spatial characteristics of deformation. This micro-DIC study is recently published [24]. It is interesting that this channel has about 15 million data points over the field at a given time whereas the IRT channel conducted on numerous separate samples is used to obtain one value at a time (the field average temperature). Note also, since the temperature is a dissipating signal, synchronous measurement of temperature and micro-strain fields is not possible.

In short, the primary goal of the study is to use infrared thermography to calculate stored energy in magnesium (unnotched dog-bone sample) due to cyclic loading. In a

separate but complementary effort, micro-DIC has been used to quantify guided and overlapped twin-driven shear bands in cross-notched samples.

2. BACKGROUND

2.1. Magnesium Deformation Mechanics with Twinning and Detwinning

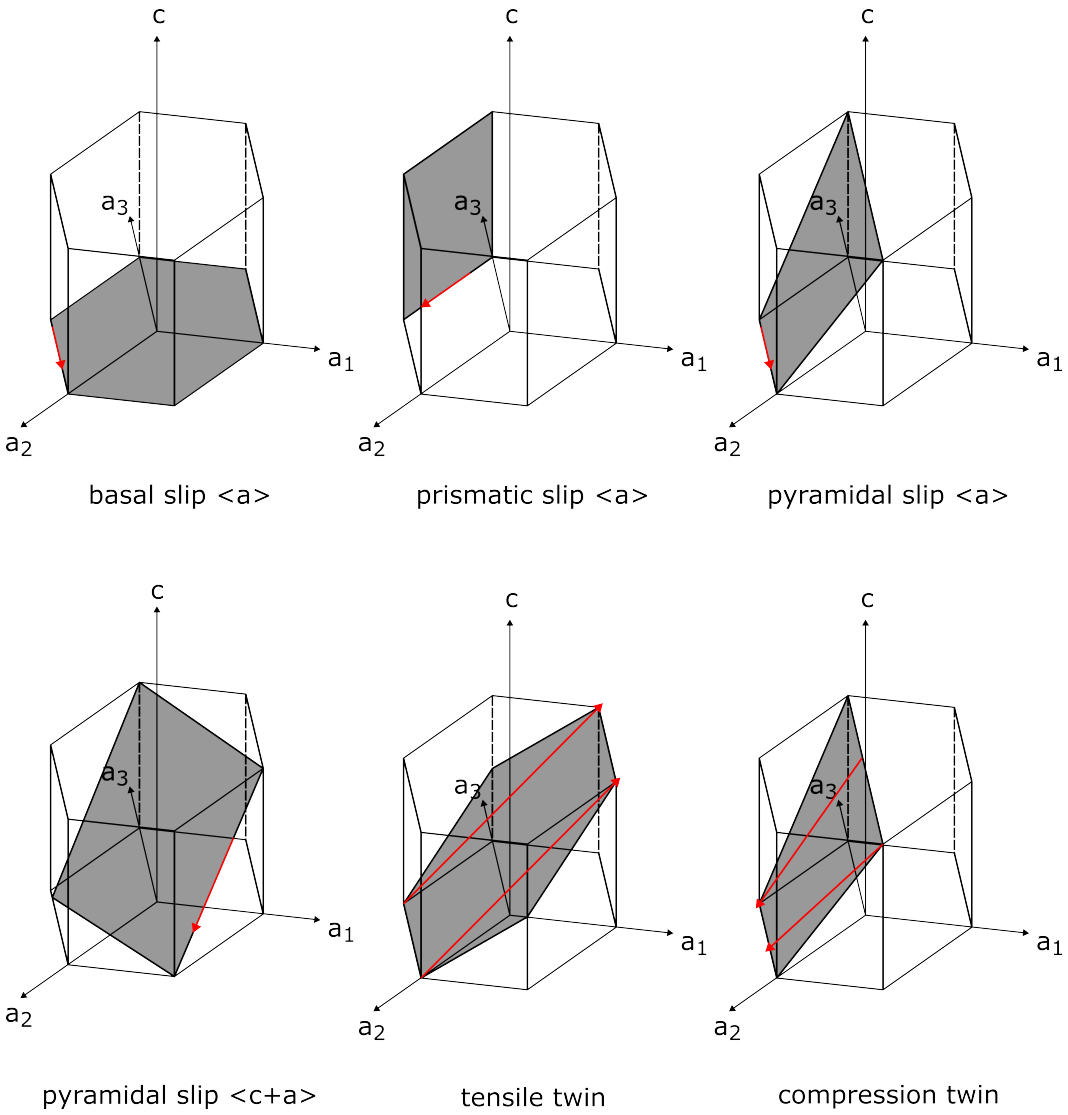

Figure 2.1. Twin and slip mechanism for magnesium over unit cell.

Figure 2.1 shows the slip systems and twin systems of HCP magnesium over an HCP unit cell. There are two types of Burgers vector in HCP metals according to its direction of motion: a and a+c. Red arrows in each HCP unit cell which are shown in Figure 2.1 indicate each system's direction of motion. Basal slip ($< 11\bar{2}0 >$ slip direction and $\{0001\}$ slip plane normal) is the most common mode in all possible slip

modes due to its low critical resolved shear stress (CRSS) [25]. In addition to four independent slip systems that can be obtained with a combination of basal $< a >$, pyramidal $< a >$, prism $< a >$ slips, the activation of $< c + a >$ pyramidal slip can meet the requirement of von Mises criterion. At the room temperature, it is difficult to activate $< c + a >$ pyramidal slip due to a high CRSS value [26]. Mechanical twinning can provide an additional mode to fulfill von Mises criterion [2]. Particularly, mechanical twinning is essential for HCPs since HCPs do not have sufficient active slip systems to accommodate strain solely with dislocation slip [27].

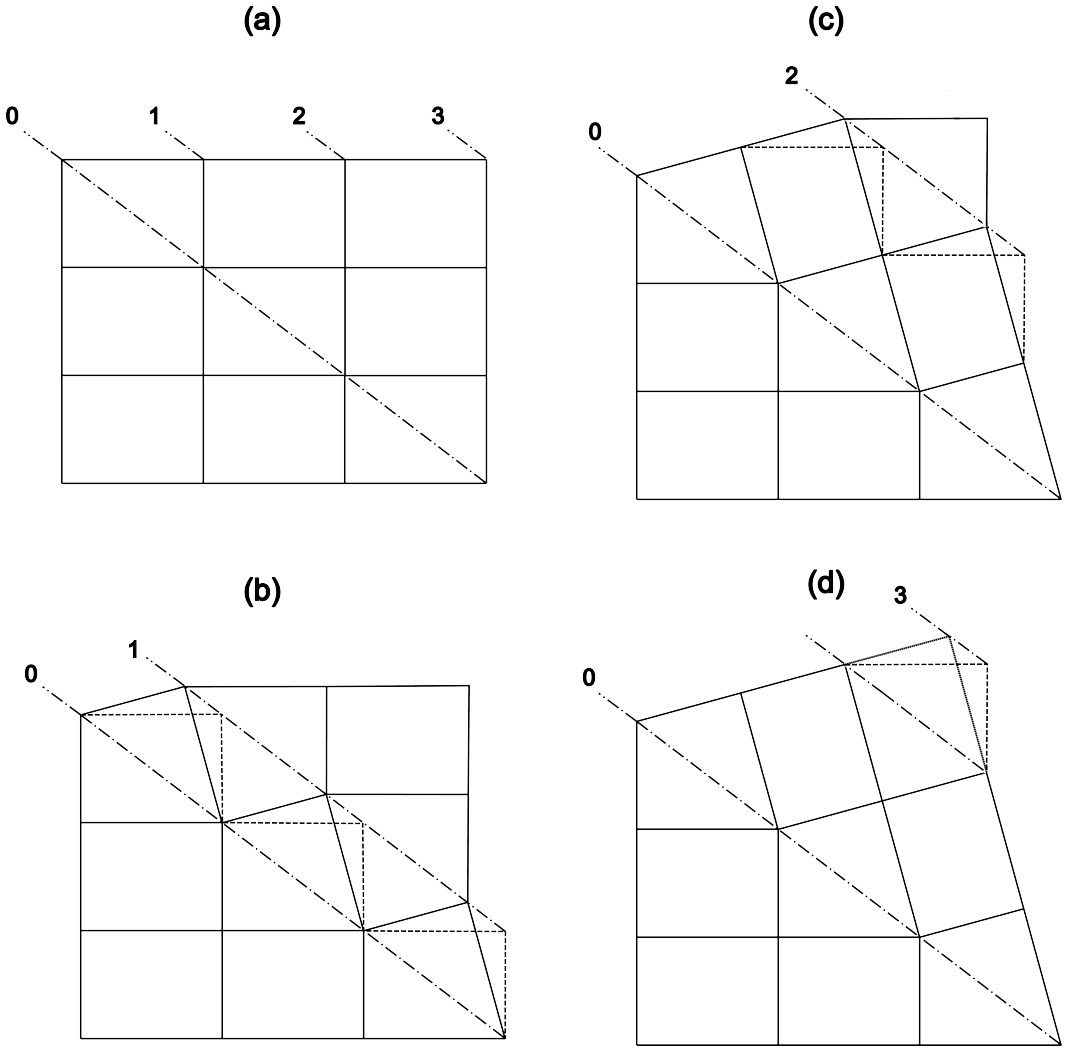

Figure 2.2. Consequtive deformation of parallel planes that undergo twinning due to shearing.

Akin to the slip mechanism, mechanical twinning occurs due to imposed shear stress. Figure 2.2 indicates uniform shearing with respect to the mirror plane (dashed line corners represent the undeformed positions, and center lines represent mirror planes). Firstly, plane 1 (shown in Figure 2.2b) experiences shear displacement relative to plane 0 (the mirror plane). The other planes undergo the same displacement relative to the former plane (e.g., plane 2 relative to plane 1 in Figure 2.2c or plane 3 relative to plane 2 in Figure 2.2d). Consequently, the new orientation that mirror symmetry with respect to the un-twinned part of the material which is seen in Figure 2.2d is produced by shear [28].

Twinning is a common plastic deformation mechanism in magnesium alloys contrary to other structural metals. There are several differences between slip and twinning [28]:

- The orientation of the lattice changes abruptly in twinning whereas lattice rotates gradually in slip.
- The activation of twinning is dependent on the loading direction (can be named unidirectional). Magnesium crystal should be loaded in a way that the unit cell is stretched along the c-axis (e.g., by c-axis tension or compression perpendicular to c-axis) to activate $\{10\bar{1}2\}(\bar{1}011)$ tensile twin systems.
- In slip plasticity, all atoms in a material move same distance, in twinning, atoms in a successive plane move different distance according to its location to mirror plane.

Detwinning is simply the reversal mechanism of twinning. The orientation of the twinned grain neighborhood turns back its original parent orientation with reverse load. The detwinning process takes place at a lower stress state compared to twinning because there is no need for nucleation. After detwinning, the c-axes of lattices turn to their original orientation. For rolled plates where the original texture is a strong alignment of c-axes with the normal direction (ND) of the plate (called the basal texture), twinning rotates c-axes in plane whereas detwinning recovers the basal texture once again [2].

With detwinning, formed twins gradually get thinner and narrower and, in some cases, eventually disappear completely.

2.2. Experimental Investigation of Twin Driven Deformation

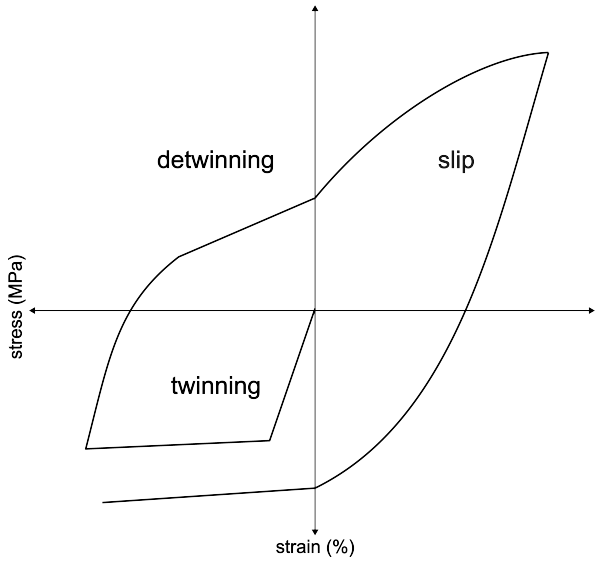

Figure 2.3. Asymmetric stress strain curve of cyclic loading of rolled Mg AZ31.

$\{10\bar{1}2\}(\bar{1}011)$ twinning is an essential deformation mode for magnesium that has low symmetry in its lattice. Twinning can be easily activated by applying compression along rolling direction (RD) or transverse direction (TD) (that causes extension along the c-axes of the crystallites). In fact, except basal slip [2], it has lower CRSS than the slip mechanisms of magnesium (AZ31).

Figure 2.3 shows the characteristic cyclic stress-strain curve of wrought Mg AZ31 when the cycle is first started in compression. The first quadrant of the loading curve represents twin-driven deformation. If rolled/extruded material is compressed along the rolling/extrusion direction, material exhibits low strain hardening, twin-driven, plastic deformation. This flat (low hardening) curve in this region is also called the "twin plateau". Once the load is reversed to tension, wrought magnesium exhibits an untypical sigmoidal stress-strain curve due to detwinning. Once strain becomes positive along with stress (right top quadrant) final quadrant, heavy hardening region

is observed since the unipolar tensile twin does not operate in this load sense and the material has to accommodate strain by hard slip plasticity modes like prism and prismatic. If the material is compressed again through RD, it shows the second twin plateau like the first part of the curve, though with slight cyclic hardening (namely, a higher stress value for the second twin plateau).

As previously mentioned, mechanical twins form in a single grain abruptly, and the resulting local stress jump might trigger twinning in its neighbors (causing autocatalytic activity). Thus, the resulting sequential activity of twinning leads to strain localization at a macroscopic scale in the form of a shear band [29]. This localization pattern is analogous to the Lüders banding structures that are well established in low carbon steels.

The observation of twin-driven macroscopic shear bands at a microscopic scale has been useful in revealing the twin network. Aydıner and Telemez [12] investigated these bands with high resolution (0.2 µm/pixel) optical microscope. The study reveals individual twin deformation events by overlapping high-resolution strain maps with the underlying microstructure. Also, this study contains two-orthogonal-surface measurements that present the 3D behavior of shear bands. DIC is conducted at optical microscopy resolution but also over a very large field of the material (coverage about 104 grains) yielding a combination of macroscopic coverage and microscopic resolution. An improved version of this method (DIC with area-scanning optical microscopy) has later been applied in non-twinning load paths [20] and under cyclic loading [13] as well. A complementary study with macroscopic DIC (Kapan et al. [14]), highlights the primary role of texture on the sharpness of the twin-based shear bands at the macroscopic scale.

Rolling texture of the magnesium under in-plane compression has been observed to be the worst case for the severity of the shear band, whereas extruded material with transverse isotropy yields less compact strain localization structures. The severity of shear bands also depends on the load history (e.g., the second compression after a cycle of compression-tension loading compared to the original compression). Shafaghi et

al. [13] revealed the compactness difference of shear band families (e.g., ± 45° shear band families) over such consecutive twin plateaus in cyclic loading. Even if the kinematics of the second wave bands are equivalent to those of the first wave bands, the second wave strain content is more diluted than the first wave (particularly due to the interaction with preferential slip structures that are called non-45° bands in Üçel et al. [20].

2.3. Infrared Thermography in Mechanics

IRT is a non-contact method that enables real time in situ measurement over continuously loaded samples. There is no need for any other special equipment for IRT based monitoring [30] except the thermal camera. IRT is widely classified into two major classes: passive thermography and active thermography. In passive thermography, sample investigation is conducted without external heat sources because the sample is considered a heat source. On the contrary, in active thermography, external heat stimulations are fundamental to the system [30]. In our cases, the deforming sample acts as a heat source (as part of the plastic work is converted to heat), and our case can be characterized passive thermography. The temperature variation caused by this heat source is quantified with IRT.

Material deformation has a temperature signal. This temperature change in part stems from material volume change. There is a reverse relation between volume increase and temperature increase. Even elastic deformation in compression increases the temperature of the material, elastic deformation in tension decreases [31]. Heat generation during elastic deformation ($\dot{Q}^e$) can be understood with the sign of elastic strain rate tensor in this formula

$$\dot{Q}^e = -\frac{\alpha}{\rho c_p}(3\lambda + 2\mu)T_0\underline{\underline{\dot{\varepsilon}}}^e, \tag{2.1}$$

where α is thermal expansion coefficient, T_0 is initial temperature, λ and μ elastic constants, $\dot{\varepsilon}^e$ elastic strain tensor rate. The volume change effect is more associated with elastic behavior since plastic processes (such as slip and twinning) are simple shear processes that are isochoric.

Heat generation during plastic deformation however is due to plastic work done on the sample and can be calculated like through

$$\dot{Q}^p = \underline{\underline{\dot{\varepsilon}}}^p \beta \underline{\underline{\sigma}}, \tag{2.2}$$

where $\underline{\underline{\sigma}}$ is stress tensor, β is Taylor-Quinney coefficient, and $\underline{\underline{\varepsilon}}^p$ is plastic strain rate tensor.

The fraction of plastic work converted to heat that is dissipated from surface is named Taylor-Quinney coefficient (β). Even if a portion of heat is stored in material (store means changing the internal energy, e.g., by increasing the number of crystal defects), a great majority is converted to heat, increasing the temperature of material [32]. Under adiabatic conditions, Taylor-Quinney coefficient can be calculated with

$$\beta = \frac{\rho c_p \Delta T}{W_p}, \tag{2.3}$$

where ρ is the density, c_p is the heat capacity of the material, ΔT is the temperature change during deformation, and W_p is the total plastic work.

Thermo-mechanical coupling for routine plasticity has been typically investigated at high strain rates because there is no time for heat to escape (adiabatic process) from deformation zone to undeformed zone [32, 33]. In a short period of time, plastic work transforms heat that is released from deformation zone [34] and temperature measurements with IRT is conducted to quantify this heat. The high-strain rate studies over twinning magnesium alloys are recent and rare [35, 36] and mechanisms for the observed results demand further investigation.

2.4. On banded structures with IRT measurement

Heat generation can be addressed for different types of deformation mechanisms. Mechanical behavior of engineering materials is affected from the associated temperature increase. As a case study, consider Portevin-Le Chatelier effect that is a form of plastic instability that causes an increase in strength but decreases the ductility in some steels and aluminum alloys. In this deformation mode, strain heterogeneity is observed like

Lüders band structure over gage length. A correlation between temperature increase and band nucleation in this deformation mode has been observed [37]. In another study, Al 3.2% Mg sample is loaded in tension to characterize the thermal behavior of Portevin-Le Chatelier effect at different strain rates. Infrared thermography is employed with 0.02°C noise level to detect temperature change in this work [38].

Temperature and strain field heterogeneity are studied in an austenitic stainless-steel sample that contains hundreds of grains in tension with different strain rate [39]. At the same stress level temperature gradient is higher in high strain rate ($5x10^{-3}s^{-1}$ - 0.25 °C) experiment compared to low strain rate ($5x10^{-4}s^{-1}$ - 0.15 °C) experiment. Furthermore, when two sequential stress level over plastic regime (approximately 5 MPa difference is valid) is investigated, local temperature increase is observed in corresponding region that experience strain increment [39].

2.5. Infrared Thermography Uniaxial Testing

IRT is used to characterize thermal behavior of the unnotched magnesium AZ31 sample under cyclic loading in this work. However, the conditions cannot at all be assumed adiabatic given the limited strain rate and highly conductive metal sample.

A more detailed treatment of the energy budget is necessary. The aim is to separate stored energy during elastic and plastic regions which is driven by twinning, detwinning, and slip. There are several factors to consider energetic aspects during plastic deformation in terms of thermodynamic effects. Based on the conservation of energy principle, the heat equation can be deduced. The main formulation that will be used toward this goal is an expression of the first law of thermodynamics [40]

$$\rho c_p \dot{T} - div(q) = \Delta + r + \rho T \frac{\partial^2 \psi}{\partial T \partial \underline{\underline{\varepsilon}}^e} : \dot{\underline{\underline{\varepsilon}}}^e + \rho T \frac{\partial^2 \psi}{\partial T \partial V_k} : \dot{V_k}. \tag{2.4}$$

- $\rho c_p \dot{T}$ represents the heat rate due to temperature variation: in which ρ and c_p are mass density and specific heat capacity.
- $div(q)$ represents the heat rate losses due to conduction.

- $\Delta = \underline{\underline{\sigma}} : \dot{\underline{\underline{\varepsilon}}}^p - A_k : \dot{V}_k$ represents the internal dissipated energy, where $\underline{\underline{\sigma}}$ is stress tensor, $\underline{\underline{\varepsilon}}^p$ is non-linear part of the strain tensor, A_k indicates a set of thermodynamics forces related to a set of internal variables V_k.
- r represents the external heat supply (zero in our passive measurement).
- $\rho T \frac{\partial^2 \psi}{\partial T \partial \underline{\underline{\varepsilon}}^e} : \dot{\underline{\underline{\varepsilon}}}^e + \rho T \frac{\partial^2 \psi}{\partial T \partial V_k} : \dot{V}_k$ represents thermodynamic coupling sources. ψ denotes the specific Helmholtz free energy.

Also, it should be mentioned that there are some assumptions in formulating Equation (2.4).

- It is stated that ρ and c_p are material constants and are not affected by temperature.
- Convective terms (in material time derivatives) are neglected.
- It is assumed that r is time independent.
- Also, heat generation during plasticity is considered an irreversible process.

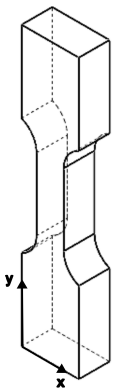

Figure 2.4. x-y coordinate system on the dog-bone sample.

Following the treatment in reference article [40], next Equation (2.4) is simplified to use terms that are measured in our experiments. The dog bone sample that is used in the cyclic experiment has a uniform cross-section. Figure 2.4 shows the x-y coordinate system on the sample. When we consider the geometry of the sample, the height of the sample (y-direction length) is considerably higher than the width of the sample (x-direction length) at the gage section. Thus, assume that temperature varies only along y-direction). By using Fourier's law with an isotropic thermal conductivity to

model the local conduction and then also ignoring the spatial variation in temperature in the 1D gage volume altogether (This model where gage volume temperature only varies with time is called a 0D model, justified in our case by the high thermal conductivity of Mg.), reference article [40] goes on to characterize the heat loss from the gage section in terms of a (measured) characteristic time (τ_{eq}) of the sample. τ_{eq} is a characteristic time constant for the material which represents its duration to reach stable temperature [40]. τ_{eq} can be calculated experimentally from cooling curve of the sample with fitting an exponential function [41]. A sample graph will be presented in the Section 4.2.1 for loading state. The major factor for heat loss in our experiments will be conduction from the grip contacts that will also most heavily influence the value of τ_{eq}.

According to the literature, the 0D approach is also the typical approach in thermal investigation of fatigue (under cyclic loading). Characteristic time can be calculated theoretically in this formula for the 0D approach [40]

$$\frac{1}{\tau_{eq}} = \frac{2h_1(e+l)}{el} + \frac{2h_2}{L}, \tag{2.5}$$

where h_1 air film coefficient, e and l the thickness and width of the sample, and h_2 is the film coefficient between grips and specimen. The conduction term ($div(q)$) in the Equation (2.4) can be written like that for 0D approach

$$\frac{\rho c_p \Delta T}{\tau_{eq}}. \tag{2.6}$$

The other simplification of Equation (2.4) is done in thermodynamics coupling terms. It is assumed that thermo-mechanical coupling sources on internal variables, V_k, are negligible, and only thermo-elastic part can be considered. Stress tensor can be deduced from partial derivative of Helmholtz free energy as follows

$$\rho \frac{\partial \psi}{\partial \underline{\underline{\varepsilon}}} = \underline{\underline{\sigma}}. \tag{2.7}$$

Therefore $\rho T \frac{\partial^2 \psi}{\partial T \partial \underline{\underline{\varepsilon}}^e} : \dot{\underline{\underline{\varepsilon}}}^e$ can be simplified to $T \frac{\partial \underline{\underline{\sigma}}}{\partial T} : \dot{\underline{\underline{\varepsilon}}}^e$. After using Hooke Law expression for thermo-elasticity, thermo-elastic coupling will be written to

$$-\alpha T(\dot{\sigma} - 3\kappa\alpha\dot{T}), \tag{2.8}$$

where κ represents bulk modulus. Finally, Equation (2.4) can be written for our case to

$$\rho c_p \dot{T} + \frac{\rho c_p \Delta T}{\tau_{eq}} = \beta \sigma \dot{\varepsilon^p} - \alpha T(\dot{\sigma} - 3\kappa\alpha\dot{T}). \tag{2.9}$$

3. MATERIALS & METHODS

3.1. Sample Specifications

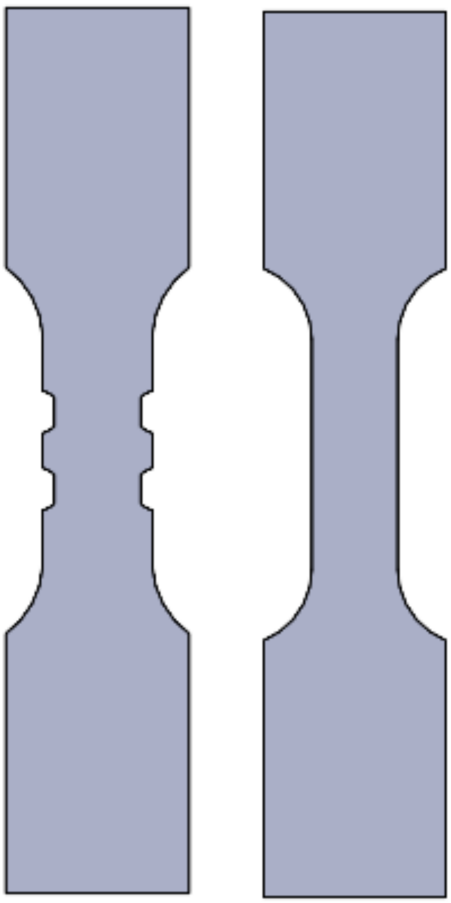

Figure 3.1. Representation of sample geometries.

In this project, there are different types of specimens: cross-notched and unnotched specimens which are shown in Figure 3.1. Magnesium AZ31 dog-bone specimens are cut via electrical discharge machining (EDM) from a 6.35 mm thick hot rolled plate along rolling direction (RD) (procured from Alfa Aesar) and from a 22 mm diameter hot extruded rod along extrusion direction (ED) (procured Xi'an Yuechen). The average grains sizes are approximately 10 µm and 13 µm, respectively. The grain size of specimens is measured by the lineal intercept method.

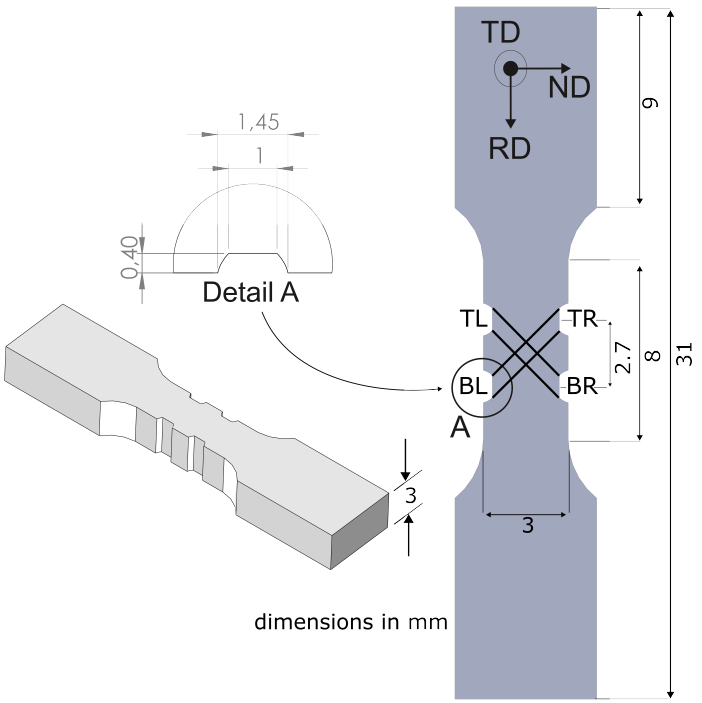

Figure 3.2. Representation of sample geometries.

The unnotched dog bone sample is loaded in a cyclic way to reveal the thermal behavior of magnesium AZ31 (in Section 4.2). Additionally, cross notched samples in both extruded and rolled are loaded in compression up to -2% axial strain to investigate twin-driven shear band characteristics with the separate micro-DIC study (in Section 4.1). The thickness of the cross-sections is kept thick relative to the gage length in both lateral directions to prevent buckling failure of the specimens.

Let us consider the notched sample (micro-DIC study) methodology first. In the twinning regime of rolled magnesium, the initial point of the shear bands cannot be predicted before the experiment. Shear bands are guided by making notches that are located at the extension of each other at an angle of 45^{o}. This is why the notches in the projected sample are offset for the rolled sample. The 0.4 mm deep notches are positioned in a cross pattern at the center of the sample. The internal width of the sample is 3 mm (shown in Figure 3.2).

Notch configuration is specified to guide and overlap twin-driven shear bands on the intended location. The relation between these bands is investigated over the middle of the observation surface.

As described in Section 1.2 of the thesis, notched samples were initially geared towards the thermal wing of the project. However, due to multiple reasons, no spatial resolution could be discerned in the thermal measurements over notched samples. To avoid unnecessary complexity, the thesis will consider unnotched samples for in situ IRT measurements.

3.2. Material Texture

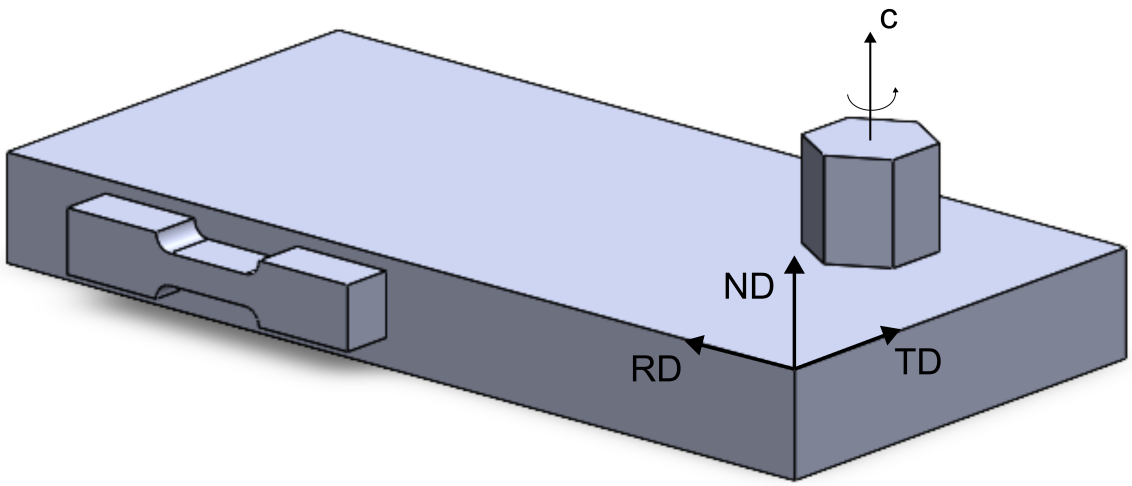

Figure 3.3. Representation hot rolled plate and the hexagonal unit cell with coordinates: rolling direction, transverse direction, normal direction is denoted as RD, TD, ND.

The basal plane of the hexagonal closed packed (HCP) lattice is parallel to the rolling direction and c-axis of the hexagonal lattice is coaxial with the normal direction (ND) of the plate that can be seen in Figure 3.3. In the extrusion material, c-axes of lattices coaxial with radial direction and ED of the rod is parallel to the basal plane lattices. Specimens are loaded in compression along the rolling/extrusion direction to trigger $\{10\bar{1}2\}(\bar{1}011)$ tensile twin system.

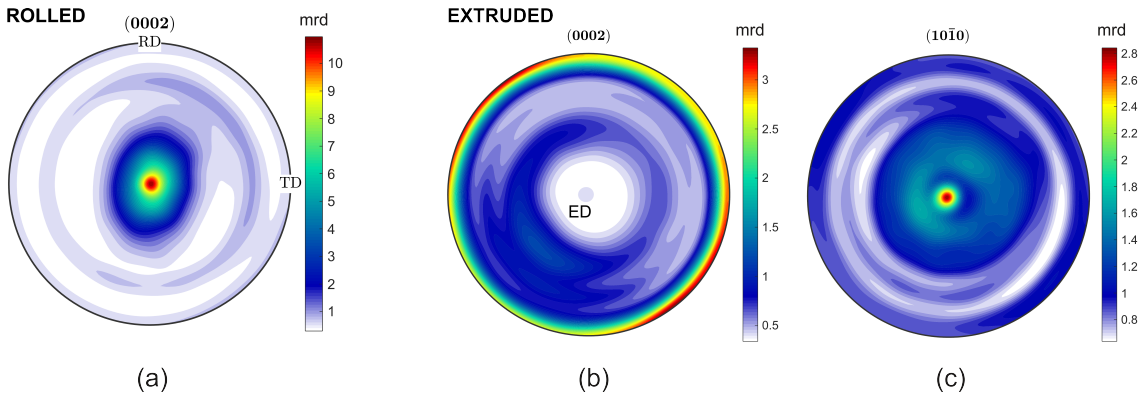

Figure 3.4. (a) 0002 pole figure for rolled material, (b) 0002 pole figure for extruded material, (c) 10$\bar{1}$0 pole figure for extruded material.

The crystallographic texture of both materials was evaluated with x-ray data from a Panalytical X-Pert Pro MPD four-circle diffractometer. Pole figures (shown in 3.4) are generated with MTEX [42] software. Figure 3.4a clearly shows the typical orientation of rolled material where c-axes are aligned with ND of the plate. Also, Figure 3.4b and c illustrates the orientation of extruded material: axis symmetrical distribution of c-axes normal to extrusion direction (ED) of the rod.

3.3. Sample Preparation

The sample preparation procedures are completely distinct for the notched sample micro-DIC experiment and the thermal experiments. These are described in separate subsections in the following.

3.3.1. Sample preparation for micro-DIC

The sample observation surface is prepared to reveal microstructure. Twins will disturb the surface morphology. Metallography processes reveal grain boundaries and yield a morphological background to the observed strain fields (e.g., strain localization fields following grain boundaries or twin-based strain bands to be consistent with the domain of the grain that a particular twin forms in). Also, metallography is necessary to

measure the grain size by linear intercept method for material characterization. There are four steps for metallography procedures. After these stages, a speckle pattern is added to the observation surface to increase its contrast for DIC calculations.

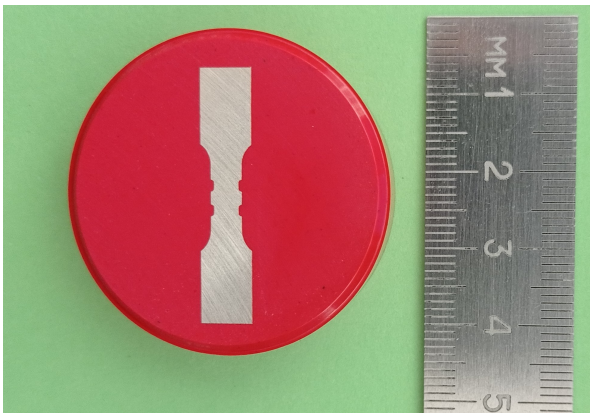

Figure 3.5. Cross-notched sample in a bakelite mold.

3.3.1.1. Hot Mounting. The specimen is mounted in a bakelite via ATM OPAL 410 hot molding machine to perform the grinding stage non-destructive and successful way. The surface flatness of the sample cannot be provided without molding the sample. There are several optimum parameters for the hot mounting process, such as 5 minutes for curing time, 4 minutes for cooling time, 150°C for temperature, and about 10 MPa for pressure. The molded sample is placed into ATM SAPHIR 530 automated grinding machine in the next stages. The molded cross-notched sample with a ruler is shown in Figure 3.5.

Another important issue is extracting the sample from the mold in a non destructive way since this is the actual sample, we will conduct experiments and one must avoid pre-deforming the sample before the loading experiment. For this purpose, a piece of aluminum foil is placed into the back surface of the sample during the hot mounting process to create an (easy to separate) interface between the sample and the mold material. The mold material around the sample is first cut via bandsaw with a safe margin. Then delicate mechanical operations are continued to extract the sample from the mold.

3.3.1.2. Grinding. The sample is placed into the automated grinding machine to remove a layer of material that is generated during EDM cutting from the sample surface. The sample surface is grinded sequentially with P1200 (for 2 minute), P2400 (for 4 minutes), and P4000 (for 8 minutes) waterproof grinding paper to remove EDM layers. Surface flatness should be ensured in the grinding stage since, otherwise, the accuracy of the DIC measurements is compromised. (When the sample is tightened in compression-tension module, its observation surface needs to be orthogonal to the fixed optical elements. Otherwise, focus will be compromised, and artificial strains are introduced.) The grinding duration of the finer paper is determined by multiplying the duration of the former (coarser) paper by two.

3.3.1.3. Polishing. The flatness of the surface is improved by using oil-based colloidal silica with 0.06 µm sized particles and appropriate polishing cloth (QATM Galaxy Omega) for fine polishing. If the water-based polishing liquid is used, the surface of the magnesium samples is covered with a white layer and is not polished properly. When the polishing is continued by an automated grinding machine, colloidal silica is added by syringe. Also, ethanol is sprayed in a specific internal to clean the surface to prevent clustering silica particles on the surface. Surface scratches that originated at the grinding stage should be eliminated in the polishing stage.

3.3.1.4. Etching. The sample is dipped in a chemical etchant to reveal grain boundaries. Etchant interacts with the specific part of the surface and reveals grain boundaries. The composition of the etchants is: 0.64 gr picric acid, 1.5 ml distilled water, 1.5 ml acetic acid, and 15 ml absolute ethanol. The sample surface should be interacted with the etchant for 2-3 seconds. After that, the sample surface should be washed ethanol immediately.

3.3.1.5. DIC speckle pattern. Multi-scale (micro and macro) DIC is utilized to investigate strain accommodation in this work. DIC tracks the surface features introduced by using an airbrush (Iwata Custom B) to measure the displacement/strain fields. Figure

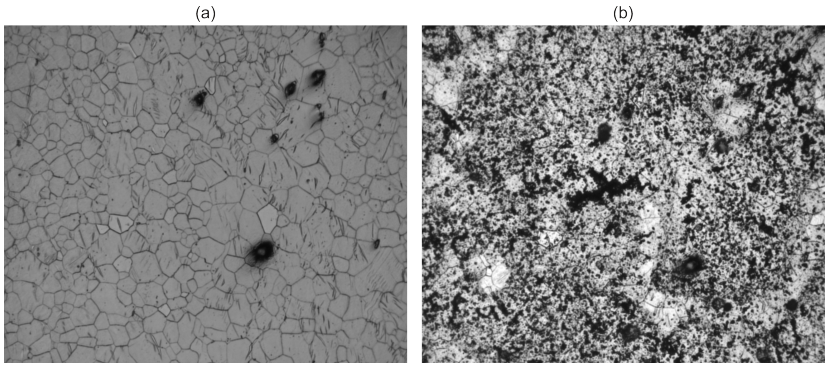

Figure 3.6. (a) a single micro frame, (b) same neighborhood with (a) with speckle addition.

3.6 shows the same grain neighborhood (with images recorded under the microscopic DIC line) before and after the speckle application. A paint mixture that contains 3 ml ethanol and 1 droplet of paint is sprayed to the sample surface from 15 cm away for 3 seconds. Ethanol is utilized in a mixture instead of distilled water to minimize surface wetness. The air pressure used in the inlet of the airbrush is set to 3 bars.

3.3.2. Sample preparation for IRT

In IRT measurements, it is critical to employ a reference sample (identical to the deformed sample in terms of surface quality and processing but that does not undergo deformation) to get accurate temperature data [34], by eliminating thermal camera detector noise. The data collected as the difference of the deformed and undeformed sections, hence, single out the minute signal due to deformation.

For this reference, a magnesium part (leftover from the EDM cutting) is attached to the side surface of the sample (Figure 3.7). Both specimen and reference surface are painted with matt black spray paint to increase observation surface emissivity. After initial experiments, we observed that the generated the deformed gage volume is in part conducted to the stress-free reference. Therefore, the temperature of the reference part erroneously increases during the experiment. (The thermal conductivity of magnesium is relatively high compared to titanium alloys, stainless steel, carbon

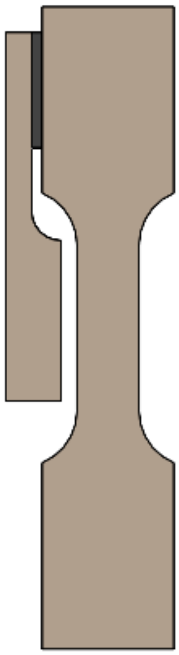

Figure 3.7. Specimen configuration for thermal measurements

steel, and nickel alloy [43]. This property causes the heat to escape from deformation zone swiftly via conduction.) Consequently, we considered putting an extra material that has low thermal conductivity with respect to magnesium between the reference part and sample for insulating the reference material. bakelite (conveniently available as it used for metallography) is used due to its low thermal conductivity compared to magnesium AZ 31 (the thermal conductivity of magnesium AZ31 is 96.4 W/m^2 [44] , the thermal conductivity of bakelite is 0.14 W/m^2 [43]). The approximately 1 mm thick bakelite insulation is glued to the sample and reference part and shown in black in Figure 3.7.

3.4. Experimental Setup

Figure 3.8 shows the formation of the experimental setup. The Kammarath & Weiss 10 kN tension-compression module (shown in Figure 3.8a) is placed top of the X/Y/Z positioning stages (Newport M-ILS series for X-Y positioning and Newport GTS30V for Z) that are shown in Figure 3.8e. Besides loading fixture has extra units

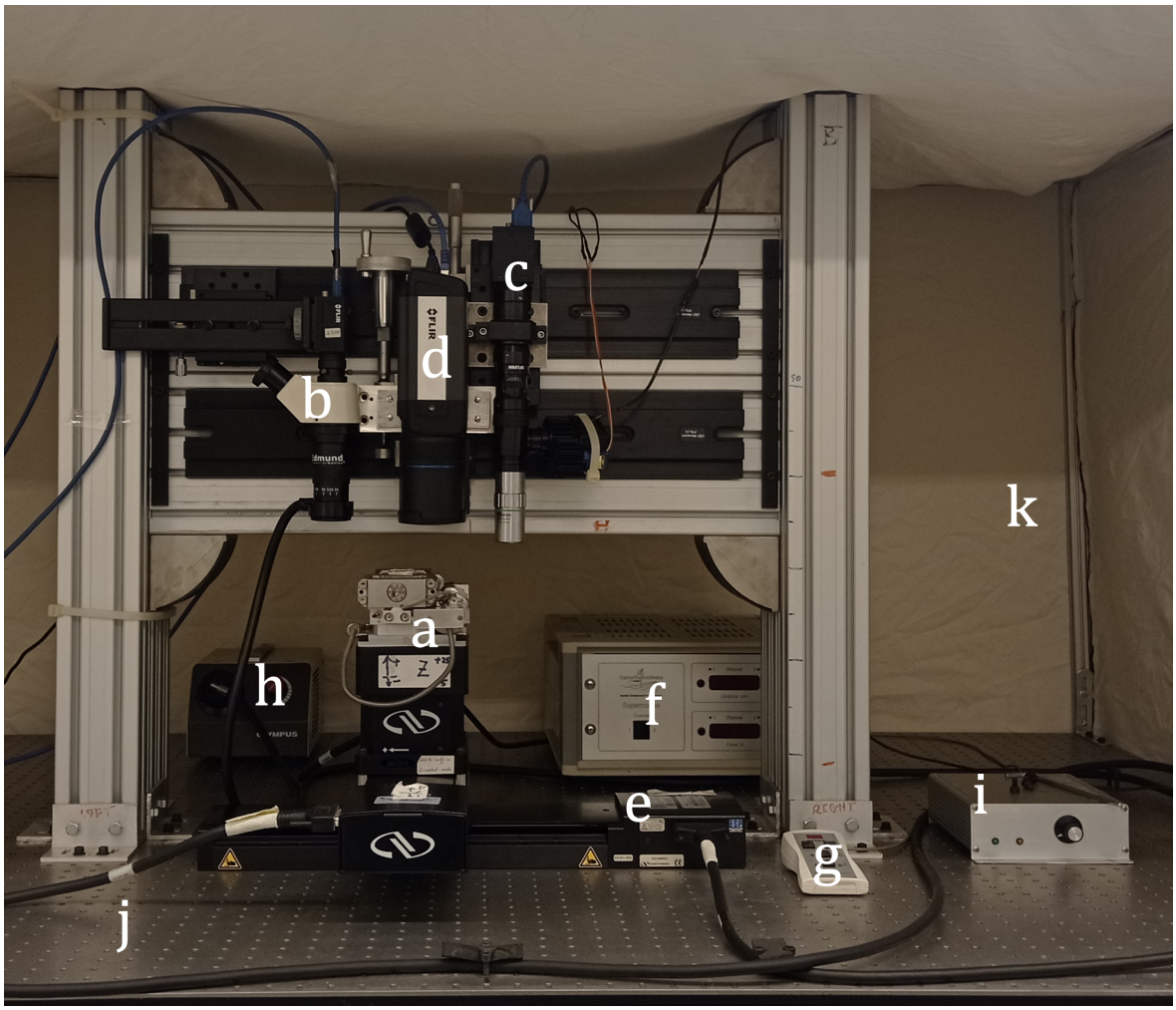

Figure 3.8. Multi-scale deformation measurement setup at the Mechanics of Advanced Materials Laboratory with elements (a) tension-compression module (b) macro-DIC line, (c) micro-DIC line, (d) IRT camera, (e) x-y-z positioners, (f) load display unit, (g) load controller, (h) macro-DIC light, (i) micro-DIC light, (j) vibration isolated optical table, (k) opaque curtain.

such as load display unit (shown in Figure 3.8f) and controller to increase the distance between two grips section of the module (shown in Figure 3.8g).

Figure 3.8b and c indicate the macro-DIC line and micro-DIC line respectively. Micro-DIC and macro-DIC lines that are placed vertically respect to the tension-compression module are one of the main elements in this setup to investigate deformation twinning. The micro-DIC line consists of a FLIR Grasshopper 3 camera with a 5 MP Sony IMX250 monochrome sensor and a Navitar Ultrazoom 6000 tube lens assembly with a high-resolution, long working distance Mitutoyo M Plan APO 20x objective at its tip with 0.42 numerical aperture (NA), 20 mm working distance (WD), and 1.6 µm depth of field (DOF). The nominal total magnification of the micro-DIC line is 40x. Due to the miniature size of the sample, the optics on the macro-DIC line is still a low-powered microscope (an Edmund Optics zoom inspection microscope head at 1x). The optical resolution of the micro and macro-DIC lines are 0.1 and 5.67 µm/pixel, respectively. There are two types of light sources that are halogen lamp and LED (light emitting diode) to increase exposure time via capturing macro-DIC and micro-DIC images. Figure 3.8h and i shows the light source controller for macro-DIC and micro-DIC lines, respectively. The whole setup is placed on a Newport RS4000 optical table with pneumatic vibration isolator (shown in Figure 3.8j).

Figure 3.8d indicates FLIR A655sc thermal camera with 1.5x close-up IR lens. Thermal camera can take 16-bit 640 x 480 pixels images at 50 Hz. When the window size of the image is reduced to 640 x 240, the frequency of the imaging is increased up to 100 Hz. The thermal sensitivity of the IR camera is < 0.03 °C. Crucially, the entire experimental setup is covered via opaque curtain (shown in Figure 3.8k) to block outside light during the IRT measurements.

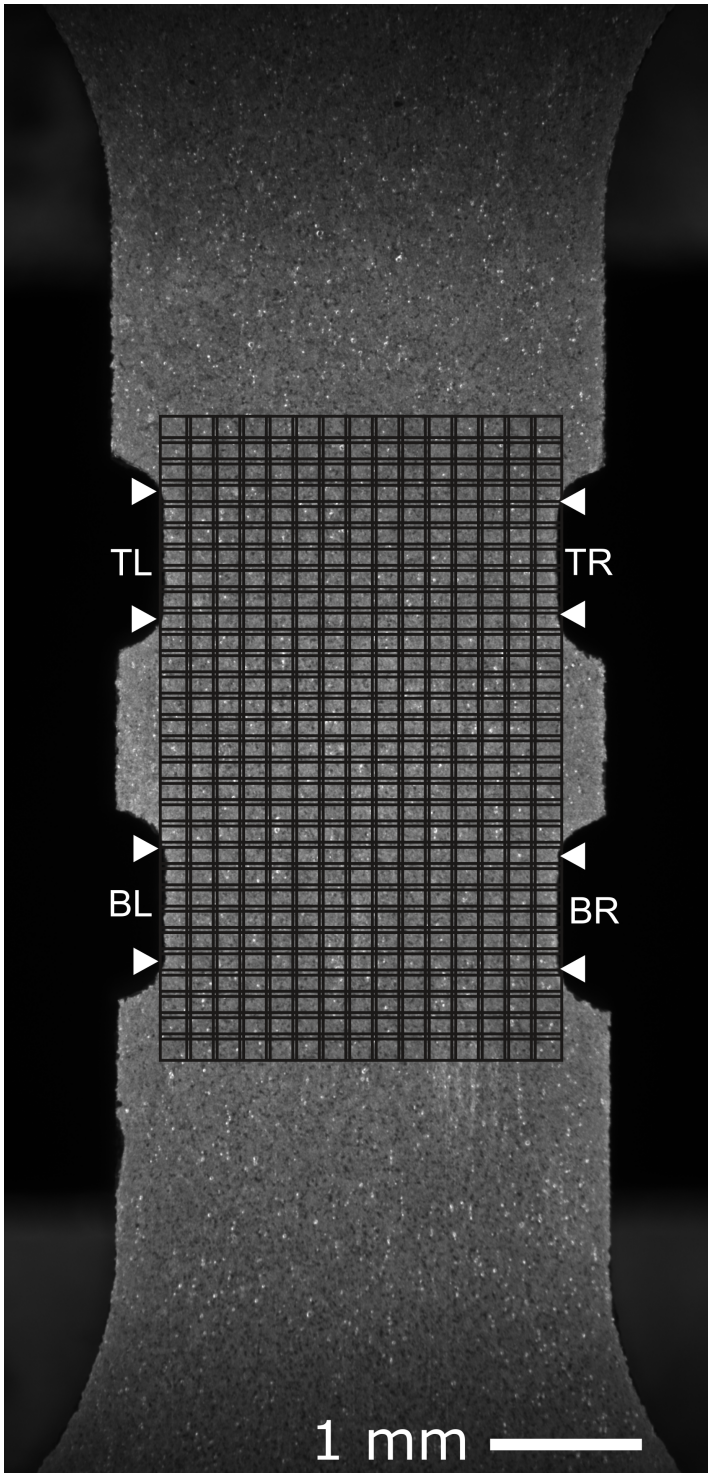

Figure 3.9. Macro-DIC image of the specimen which contains micro-DIC scan grid.

3.5. Data Collection and Analysis

3.5.1. Multi-scale DIC over the notched sample

More details on this study can be found in the corresponding publication [24]. After speckle pattern addition, the sample is placed on a flat surface and the DIC observation surface is scanned over specified grid with micro-DIC line (shown in Figure 3.9). This scan gives the x-y-z coordinates of all frames. Thus, 3D plotting of frames coordinates reveals the z-difference of corner points over x-y scan. This topography result provides a clue about surface flatness. If the specimen surface is flat enough (0.5° is the limit value for surface tilt), artificial strain can be calculated because of blurry images. Due to working low depth of field microscopy, the flatness of the surface should be maintained. After that sample is mounted into a tension-compression module to ensure the flatness of the sample along the x and y directions, and z-topography is calculated again. The surface angle is minimized up to 0.1° with successful metallography and thin metal plates addition under the linear stage.

Data recording for each micro-DIC scan takes about an hour with the automated implementation of two correction measures that are conducted at each of the 450 (X, Y) frames to maintain the DIC quality [45]. The first is WD (and thereby focus) maintenance by taking Z-stacks of images and moving the sample to the Z position that has the best focus score. (This maintains WD within a fraction of the very limited DOF.) WD maintenance is absolutely mandatory for analyzable images with the utilized high-resolution optics. The second correction pertains to the maximum preservation of the material domain in each frame [minimizing material flow to and from neighboring frames in Figure 3.9] as deformation progresses. This is achieved by an FFT-based real-time DIC analysis of the frame with respect to its previous load image and moving the sample to rectify the calculated shift. Both procedures are automated in the custom instrument software coded in Python.

The specimen is loaded in a fine strain increment to capture all twin-dominated band attacks over the twin plateau. The specimen is compressively loaded up to a -2.2% average strain in RD with fine strain increments (on average 0.0026%, 84 macro-DIC data points). The macro-DIC images are recorded at every load increment to analyze the strain field in real time. Additionally, micro-DIC area scan conducted over 30 x 15 grip by overlapping micro images at some load points (on average 0.07%, 30 micro-DIC data points). Figure 3.9 shows the micro grid overlapping macro image. The x dimension of the area-scanning grid is 0.1 mm wider than the width of the cross-notched sample at the gage section to track the initiation of the twin-driven shear bands from the notch corners. Besides, white arrows indicate notch corners in Figure 3.9. Each micro-DIC image (shown in Figure 3.10a) covers 244 x 204 μm^2 and the stitched image consists of 450 images covering 3.10 x 4.97 mm^2. DIC is performed over micro images with 10-pixel grid spacing. Grid points are indicated over small grain neighborhoods in Figure 3.10b that are also shown with blue box in Figure 3.10a. Figure 3.10c shows the speckle pattern added granular region that can be seen in Figure 3.10a with the black box. Speckle pattern addition increases the dynamic range at a pixel level. The contrast difference in pixels eases to tack material points.

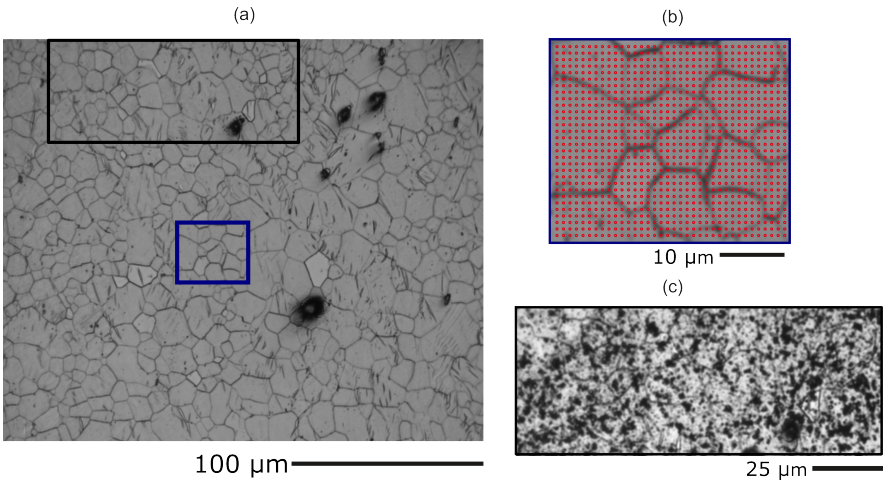

Figure 3.10. (a) a single micrograph (b) a smaller granular neighborhood (blue box in (a)) with the utilized DIC grid overlaid with red dots, (c) a speckled grain field (black box in (a)) from undeformed the scanned region. .

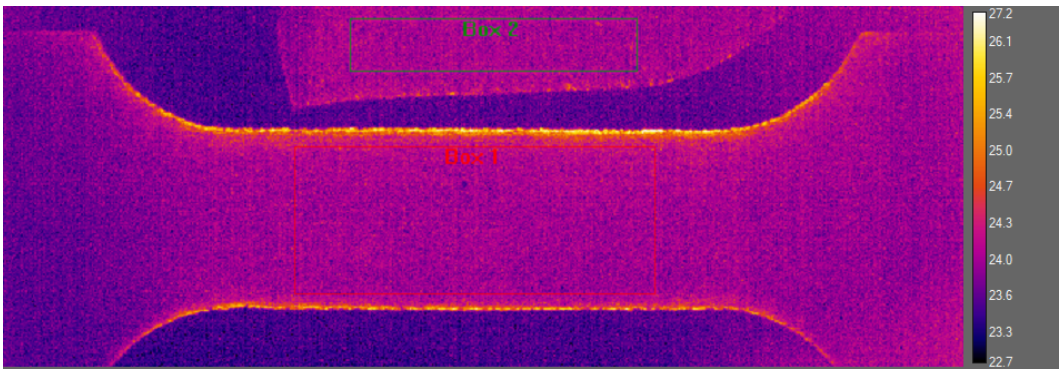

Figure 3.11. Visualization of thermal recording frame with various boxes that represent temperature field of the specimen and reference part.

3.5.2. IRT

The sample is compressed and stretched in a cyclic way to investigate the thermal behavior of magnesium. Each cycle contains compression and tension parts. In contrast to in situ experiments (strain measurements from cross-notched samples), loading is applied continues in the cyclic experiment with a maximum displacement rate of the tension compression module (20 µm/s). Load is applied in tension/compression in a specific duration that will be represented at the Section 4.2. The sample is placed in a tension-compression module in the same with in situ experiment. In contrast to in situ experiments, samples are loaded under the thermal camera. In the loading period, live IR recording is taken. The frequency of the live IR recording is 100 Hz. Sample must be loaded under thermal camera because IRT signal dissipate easily in contrast to DIC experiment. After that sample is sent to under the macro-DIC line to capture macro scale optical image. Macro-DIC images are captured before and after each compression and tension loading to compute macro-DIC analysis. Strain measurement is conducted continuously via IR images that are extracted from IR recordings. Macro-DIC images are utilized to double-check strain results that come from IR images. In addition to the IR recording, force data was collected from the loading unit via National Instrument (NI) BNC-2110 Desktop Mount Terminal Block. This device allows high-speed measurement of the load from the load cell (about 10^4 Hz).

Cyclic loading is performed under the thermal camera; consequently, thermal recording is obtained to continue further investigation to reveal the thermal behavior of magnesium. Figure 3.11 shows the classic view of the IR measurement that is taken from ResearchIR software. As previously mentioned in Section 3.3.2, the reference part is attached to the specimen by creating an insulation with glue and bakelite. Temperature field of reference and specimen is evaluated via appropriately sized boxes in ResearchIR software (shown in Figure 3.11).

3.5.3. IRT-DIC

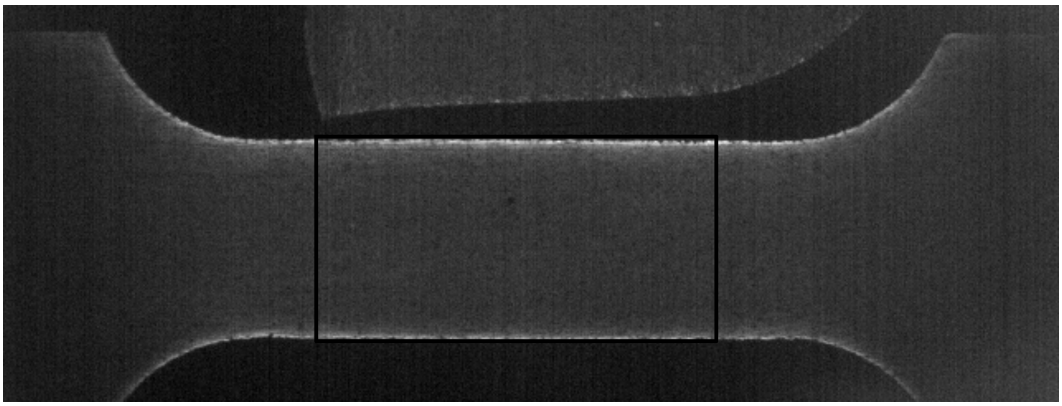

Figure 3.12. A single thermal camera frame that is used to measure strain with DIC subset.

There are two main measurement techniques in our work: optical microscopy for strain calculations and IRT measurements to understand the thermal behavior of magnesium. There are several obstacles to conducting optical investigation and IRT investigation at the same time. In situ microscopic area scanning helps to quantify the strain field and strain accommodation characteristics of the sample. Nevertheless, samples are continuously loaded under thermal camera to quantify the thermal behavior of sample in thermal experiment. There is no time to perform area scanning under a micro-DIC line during the cyclic experiment to measure the strain field. Another problem in conducting the optical investigation in addition to the IRT investigation is the mismatch in light requirements. Bright field optical microscopy used in our work requires high-intensity light whereas the thermal camera should be spared from any

external radiation sources since it measures the minute intrinsic radiation emanating from the sample. This disturbs the quality of thermal measurements. While DIC can be conducted ex-situ at the edge of each deformation cycle, extracting the actual strain at each time point (the temperature is measured every 0.01s) is critical for energetic calculations. (Sample strain does not follow the imposed linear displacement ramp of the loading apparatus due to machine compliance.) While the IRT images are not at all ideal for DIC work (in terms of pattern quality and noise), they are employed here to satisfy this need (Figure 3.12).

A single subset is assigned to the sample gage section and this subset contains sample boundaries. (Fortunately, the target is the average gage strain; spatial resolution over these images is not attainable.) Figure 3.12 shows the IRT-DIC image with the IRT-DIC subset. There are no significant features in the middle of the sample, and speckle-pattern is not of adequate quality to perform IRT-DIC. Rather, a jagged structure at the sample boundary enables tracking material neighborhood between sequential images. Recall we also captured optical images at the end of each loading, e.g., after cycle 1 compression, after cycle 1 tension, to perform macro-DIC (one of the macro-DIC images can be seen in Figure 3.14) and these constitute confirmation points to check the IRT-DIC results. More clearly, the IRT-DIC result at the last time point should be consistent with the macro-DIC result.

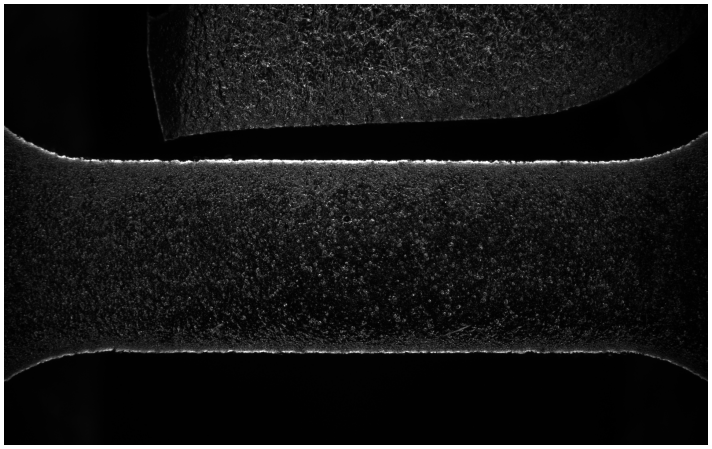

Figure 3.13. Optical microscopy image for macro-DIC.

4. RESULTS

4.1. In situ micro-DIC experiments on the cross-notched geometry

The full detail of this work has been published in *Materials Today Communications* recently [24].

Each axial strain (ε_{yy}) contour maps (shown in Figure 4.1a-k) encompass approximately $\sim 1.5 \times 10^5$ grains (sampled with $\sim 1.5 \times 10^7$ data points). These strain maps show the deformation stage of the specimen clearly. Figure 4.1l shows the engineering stress, σ, versus the axial strain averaged over the full micro-DIC field, $\overline{\varepsilon_{yy}}$,. The locations of load points that correspond to the axial strain maps are indicated over Figure 4.1l with filled red circles. The axial strain map of point i (Figure 4.1i) is selected to represent disproportionally large compared to other strain maps to express resolution and micro-scale patterning of the field. Furthermore, macro-DIC strain maps cannot indicate the intricate structure of twin-driven bands due to its optical resolution. The point i macro-DIC axial strain map is attached to the dormant region of point i micro-DIC strain maps to convey the difference of measurement scales. Also, triangle symbols that represent the corners of the horizontal section of notches are placed in Figure 4.1i, also corresponding to the white triangles in Figure 3.9. The segments between the corners are represented with flat red segments in other strain maps due to space considerations.

After the transition point of the linear section (elastic region) and nearly flat section (twin plateau), strain localization starts from notch corners with individual veins that are shown in Figure 4.1a with double black arrows. Also, there is a red arrow to indicate direction of shear band advance. In the next load point, these antecedent structures create a connection in the TL-BR corridor that is marked in Figure 4.1b with double black arrows. One of the first shear band fibers that is seen in Figure 4.1b thickness equals only 50 µm (5 grains). This emphasizes the novelties on spatial

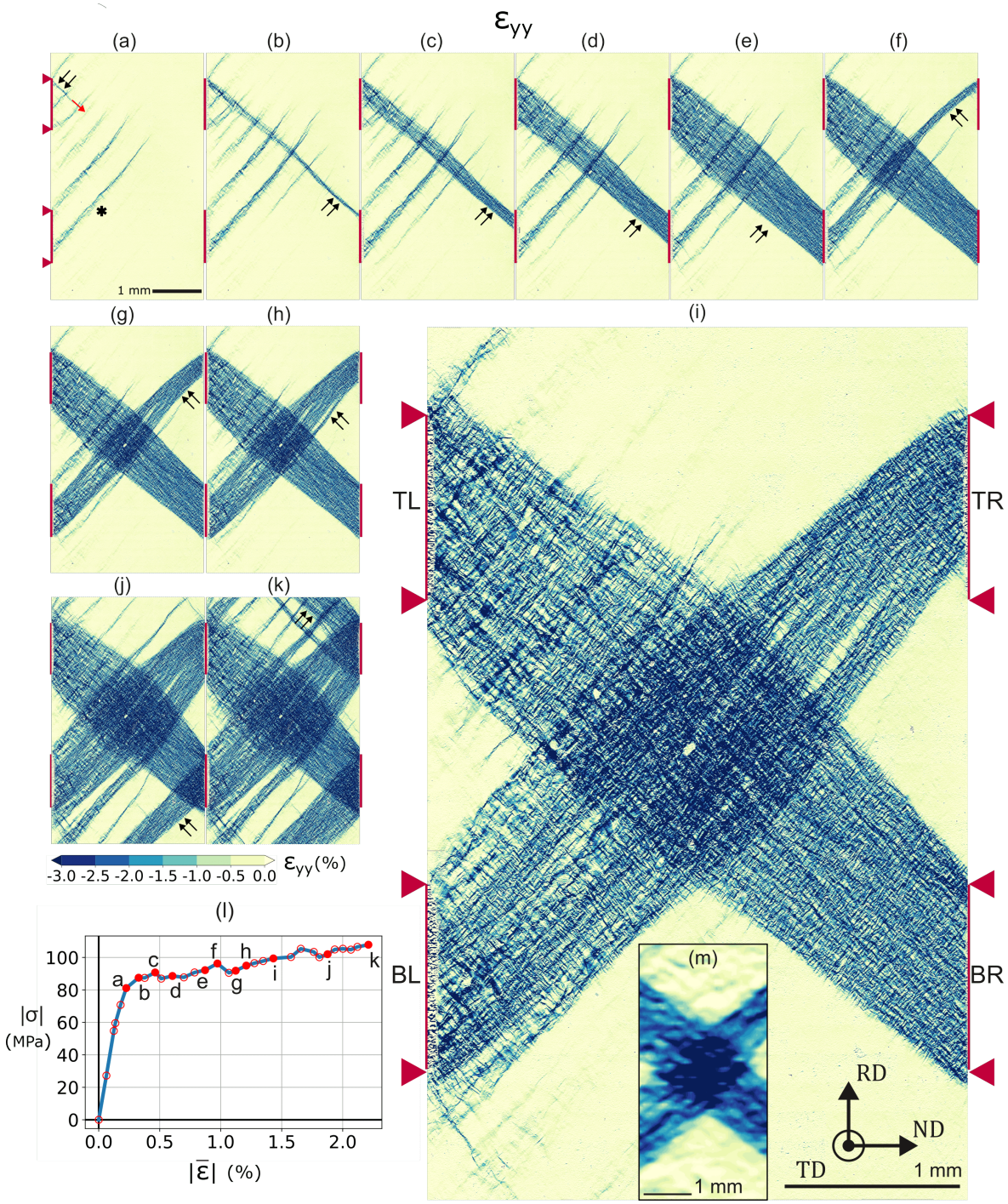

Figure 4.1. (a)-(k) Full-field (stitched) micro-DIC axial strain, (ε_{yy}), maps at load points (a-k) indicated over (l), the engineering stress versus average strain curve of the sample under compression; (m) macro-DIC (ε_{yy}) map at point i for comparison.

resolution and load/time step of measurement. After load point b, shear band formation continues its advance in -45° lateral direction that can be seen in Figure 4.1c-e with double arrows. Therefore, TL-BR corridor is filled with one set of shear band families (-45° shear band family). Then, strain accommodation along BL-TR corridor starts with the activation of +45° shear band formation. The first connection of the opposite sign shear band is completed in Figure 4.1f. This evolution supports the design target of the specimen, namely, guiding the shear bands in a cross pattern. Further evolution of opposite sign shear band is presented in Figure 4.1g-k.

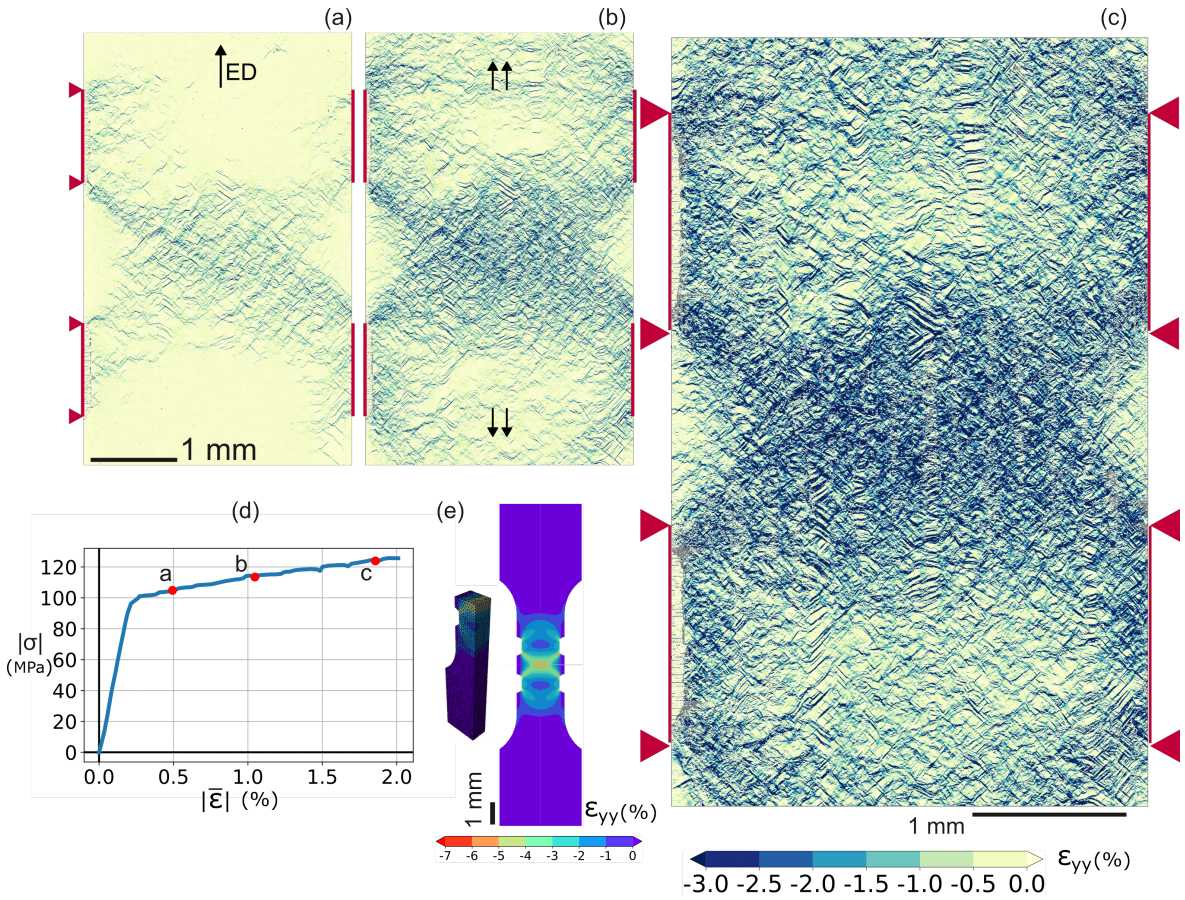

Figure 4.2. (a) - (c) Axial strain maps, (d) engineering stress-axial macro strain curve of the transversely isotropic extruded sample under compression, (e) axial strain contours (at 1.5% absolute average strain) on the surface of a 3D finite element analysis (actual analysis domain on the left) that considers isotropic Mises plasticity.

The notch configuration is designed to trigger the extremely anisotropic (with the shear planes of twins largely coincident with the (RD-TD) measurement surface)

$\{10\bar{1}2\}(\bar{1}011)$ twin bands with notches specifically carved along TD. The uniqueness of this application is tested via a control experiment in transverse isotropic extruded magnesium AZ31. The same notch pattern is introduced to the specimen and compressed along ED. Figure 4.2a-c shows the deformation stages of the control experiment. The stress-strain state of each loading point is marked in effective stress-strain curve that is shown in Figure 4.2d. Even if deformation twinning is the main deformation mode in this load path, there is no severe shear band formation due to extrusion texture, where twin shear planes are randomly distributed about ED. Note the crystallographic texture of the extruded specimen is an axis symmetrical distribution of c-axes of lattices ED (that can be seen in Figure 3.4).

After the transition point to the twin plateau, the specimen expresses homogenous strain accommodation without any clear significant localization, and the gage section is largely covered with twin patterns. Even if twin activity mostly concentrates at the middle of the specimen, there are several off-shots away from notch corners. These off-shots create a connection at Figure 4.2b and create a localization pattern that is shown with double black arrows in Figure 4.2b. This localization pattern crudely resembles the shape of the number "8". Intensity of the 8-shaped high strain zone increases in point c axial strain map ($\overline{\varepsilon_{yy}}$). 8-shape strain accommodation also agrees with simple isotropic Mises plasticity finite element (FE) analysis of this sample geometry. That means this case agrees with what is expected of a routine metal when this peculiar notch pattern is introduced. The contour plot (shown in Figure 4.2e) is obtained from FE analysis which is conducted in ABAQUS^{TM} software.

4.2. In situ infrared thermography over cyclic loading

Firstly, I used codes that are written by Rian Seghir about IRT investigation in this thesis. Figure 4.3 shows the stress-strain curve of the cyclic experiment, stress corresponding to the engineering stress (with load acquired from the load cell) and strain corresponding to the IRT-DIC averages. There are 4 cycles in this experiment, and each cycle is composed of compression and tension parts. In each wing, the crosshead position

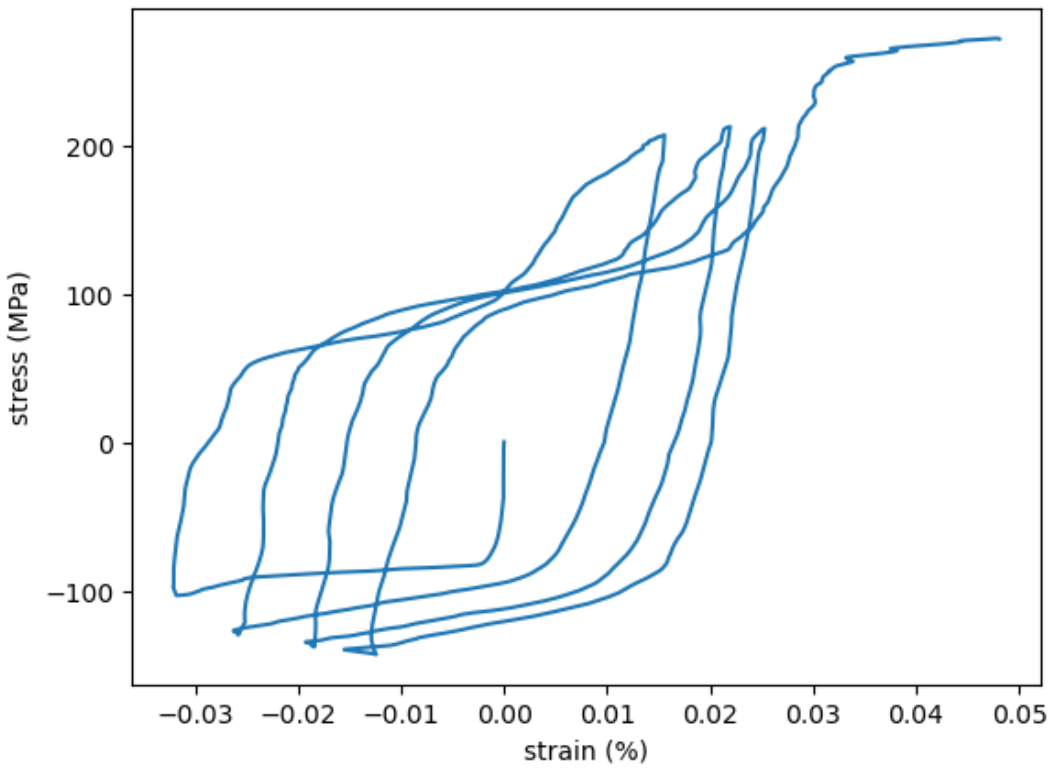

Figure 4.3. Stress-strain curve of the cyclic experiment over rolled magnesium AZ31.

has been increased linearly with the maximum speed of the load frame (20 µm/s). Table 4.1 shows details of the experiment. While durations of the linear loading segments targeted a symmetric experiment in strain, there are appreciable variations (Figure 4.3 and Table 4.2) in imposed strains in each wing likely due to machine compliance effects.

Table 4.1. Experiment details of cyclic experiment.

Cycle	**Loading State**	**Loading Type**	**Experiment Duration (sec)**
1	0-1	Compression	16
1	1-2	Tension	32
2	2-3	Compression	32
2	3-4	Tension	32
3	4-5	Compression	32
3	5-6	Tension	32
4	6-7	Compression	32
4	7-8	Tension	48

Recall thermal images that are extracted from the IR recording are used for continuous strain measurement, but macro-DIC is also employed to check strain result correctness after each loading (for this reason the same region is selected for both strain calculations). Table 4.2 shows axial strain results for each loading. For cycle 1 and cycle 2, axial strain values show similarity between both IRT-DIC and OM-DIC. After cycle 3, there is approximately 25% discrepancy between IRT-DIC and OM-DIC strain results. In this work, the emphasis is illuminating the difference of thermal behavior in compression and tension since these correspond to twinning and detwinning regimes. So, energetic calculations are confined to cycles 1 and 2.

Table 4.2. Axial micro strain averages after each loading of cyclic experiment (macro-DIC results).

Axial strain	**Value**
ε_{yy}^{0-1}	-3.20%
ε_{yy}^{0-2}	1.53%
ε_{yy}^{0-3}	-2.73%
ε_{yy}^{0-4}	1.50%
ε_{yy}^{0-5}	-2.44%
ε_{yy}^{0-6}	1.51%
ε_{yy}^{0-7}	-2.38%
ε_{yy}^{0-8}	3.69%

The maximum displacement rate of the tension-compression module (0.02 µm/s) is imposed in the cyclic experiment. Loading duration is the same in all loading states except loading states 0-1 and 7-8. 0-1 is the initial loading segment that starts at zero strain level whereas, e.g., 1-2 targets doubling the strain range from compressive side to the tensile side. In the following cycles, the sigmoidal stress strain curve is shifted right (an unwanted effect due to controlling the experiment with time rather than strain that is sadly not possible with IR measurement under dark conditions). The last cycle (loading state 7-8) is purposefully extended further into tension investigate the energy terms the in slip-dominated deformation regime.

Cyclic deformation of magnesium expresses a unique sigmoidal stress-strain curve, and the absolute value of axial strain average in loading state 0-1 (ε_{yy}^{0-1} = -3.20%) is higher than all loading states. We suspect that since the sample has the lowest yield stress here, the sample stiffness with respect to that of the machine is lowest here and more strain is accommodated over a given time duration. In contrast to the twin plateau, strain hardening is dominant in hard slip plasticity over the end of the curve.

4.2.1. Cycle 1 Compression

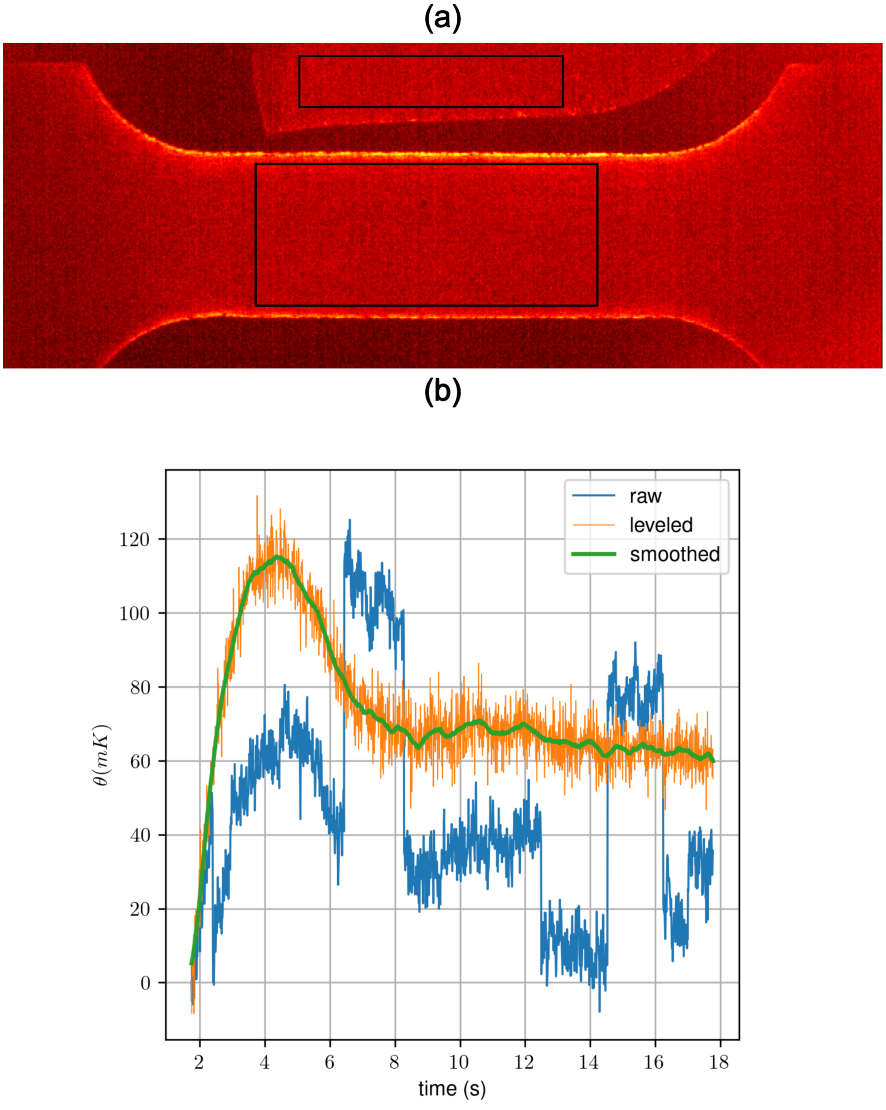

Figure 4.4. (a) Reference (top rectangle) and deformed (bottom rectangle) ROIs on a representative thermal image at the beginning of the experiment (b) Overall temperature profile in compression.

Figure 4.4a shows the initial IRT frame of the unnotched sample with deformed and reference ROIs for cycle 1 compression. Figure 4.4b shows raw, leveled, and smoothed signals for the test. IR recordings are taken to measure absolute temperature change during the test. Orange line represents the temperature difference between deformed (bottom box in Figure 4.4a) and reference (top box in Figure 4.4a) ROIs. Clearly, the unnatural jumps in the raw data are eliminated by leveling with the reference box as

shown in Figure 4.4b. Further, a Savitzky-Golay filter is employed to downscale the leveled signal to eliminate noise.

There is a temperature increase in the elastic part of the curve due to the thermoelastic response of the sample. It is clearly seen that the thermoelastic response (positive under compression, Equation (2.1)) contains a relatively higher signal compared to thermo-plastic response in compression. There is a 120 mK temperature increase in the elastic part of the deformation. There is a distinct peak during elastic deformation after which the curve attains a constant level. This means heat is still produced in the twin-driven plasticity region, just with lower signal than in the thermoelastic region. (Over other samples, it was observed that the temperature is found to drop immediately when the loading is interrupted over the twinning plateau.) The temperature fluctuation during the twin plateau might be addressed by the serrated (abrupt advances of) twin activity at this region. For examples of these sudden advances, consider the micro-DIC maps of Section 4.1.

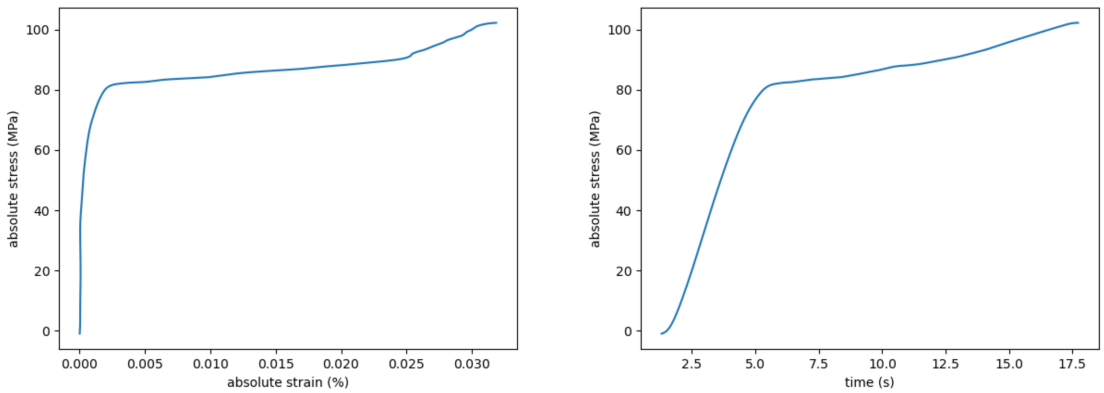

Figure 4.5. Combine stress and temperature difference curve over axial strain.

Another measurement channel for cyclic loading is force measurement. During cycle 1 compression sample is loaded up to -100 MPa. As previously mentioned, displacement rate (0.02 mm/s) and force reading frequency (10^4 Hz) is maintained for both cycles. Figure 4.5 shows the stress trend over both strain and time. The strain that can be deduced by crosshead displacement does not scale with the gage

section strain due to machine compliance. In-situ strain calculation is essential for this thesis, to model thermal behavior of the types of deformation (e.g., elastic, plastic) and deformation modes (e.g., twinning, detwinning, slip plasticity). When the crosshead displacement is considered (right graph in Figure 4.5), stress strain curve cannot be expressed correctly.

After investigating the compression and tension part in detail, energy terms will be analyzed. For this reason, τ_{eq} should be calculated, that goes into the conduction loss W_l term in the heat equation. As previously mentioned, τ_{eq} is a characteristic time constant to show time which necessary for the sample to reach stable temperature. For this calculation, the cooling profile of the first five seconds after loading is used. Figure 4.6 shows the τ_{eq} for this period.

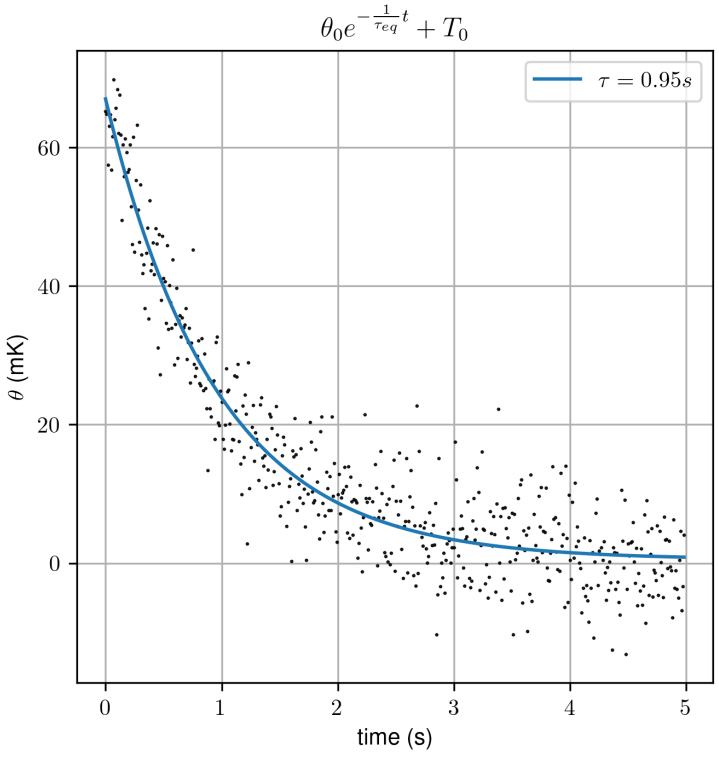

Figure 4.6. τ_{eq} calculation after cycle 1 compression.

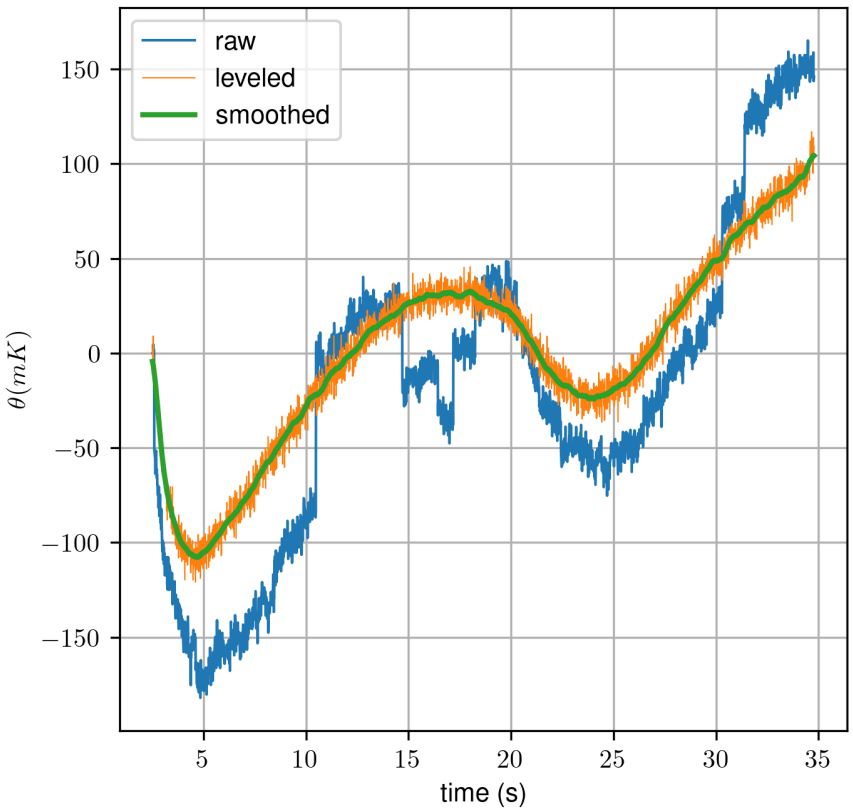

Figure 4.7. Overall temperature profile in cycle 1 tension.

4.2.2. Cycle 1 Tension

Figure 4.7 shows the temperature difference profile between deformed and reference ROIs in tension. ROIs are selected at the beginning of cycle 1, and these boxes are kept the same through analysis. Firstly, the temperature of the sample is decreased due to the thermo-elastic effect in contrast to compression due to volume increase. The temperature of the deformed region declines 100 mK because the temperature of the reference metal doesn't affect from the sample during the test. After the elastic deformation region, there is a turning point that the temperature of the sample increases up to 30 mK (there is 130 mK temperature rise in this part). Then, another temperature drop (50 mK) is observed. This temperature drop is lower than the first elastic deformation signal. After this drop, the increasing trend is maintained up to the final point of loading. Temperature increasing rate is increased continuously during slip plasticity.

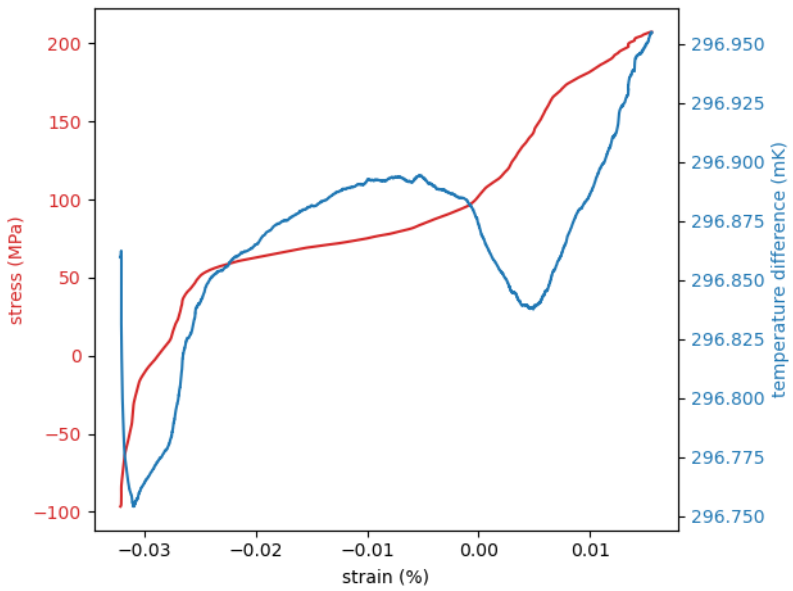

Figure 4.8. Temperature and force measurements over strain.

Figure 4.8 shows the temperature and strain measurements in the same graph over strain. After the elastic region (after -0.03% strain), the temperature of the sample increases that can be addressed to the detwinning process. After detwinning (after -0.01% strain) a second temperature drop is observed. When the slip plasticity

mechanism becomes the dominant mechanism in the test, temperature increase is observed again.

There are three turning points on the temperature profile during the tension test. The first temperature drop originates due to thermo-elastic behavior of the sample in tension. The second temperature drop is thought that another elastic deformation before the slip plasticity. This belief will be supported by energy balance in a later section. Nevertheless, a second temperature drop should be investigated deeply to relate the role of detwinning and slip systems correctly because the double-humped trend is not common behavior among slip plasticity. This deduction comes from another experiment that was conducted with a titanium sample. After the thermo-elastic response, the temperature increase is observed both tension and compression in commercially pure titanium grade 2 tests. The temperature profile of titanium and magnesium will be compared in the discussion part in compression and tension.

4.2.3. Stored energy during cyclic loading

The components of the heat equation (Equation (2.9)) are expressed into four parts

- $W_s = \rho c_p \dot{T}$: stored/released heat rate due to temperature variance.
- $W_l = \frac{\rho c_p \Delta T}{\tau_{eq}}$: heat loss because of conduction.
- $W_a = \sigma \dot{\varepsilon^p}$: imposed total plastic work.
- $W_{is} = \alpha T(\dot{\sigma} - 3\kappa\alpha\dot{T})$: thermo-elastic coupling.

W_s represents heat rate that comes from temperature variation during loading, W_l represents heat loss due to conduction, W_a represents imposed total plastic energy, and W_{is} represents elastic coupling. If the internal structure of the polycrystal remains unchanged over deformation, the total plastic work should be fully converted to heat during deformation (Equation (2.9)); therefore, Taylor-Quinney (β) coefficient becomes 1. In reality, some amount of energy is stored in a sample and does not totally dissipate

as heat. So, total plastic work W_a is multiplied with β. W_d is intrinsic dissipation, which is the amount of plastic work to dissipate to the surroundings (total plastic energy – stored energy). Also, W_b represents the stored energy which is the rest of plastic energy except dissipation during compression. W_b increases the internal energy of the material via storing in defects and dislocation pileups. W_b states stored energy during deformation. Basically, W_b should be equal to 0 if β equals to 1. Taylor-Quinney coefficient can be calculated with this formula specific to this test

$$\beta = \frac{W_s + W_l - W_{is}}{W_a} = \frac{W_d}{W_a}. \tag{4.1}$$

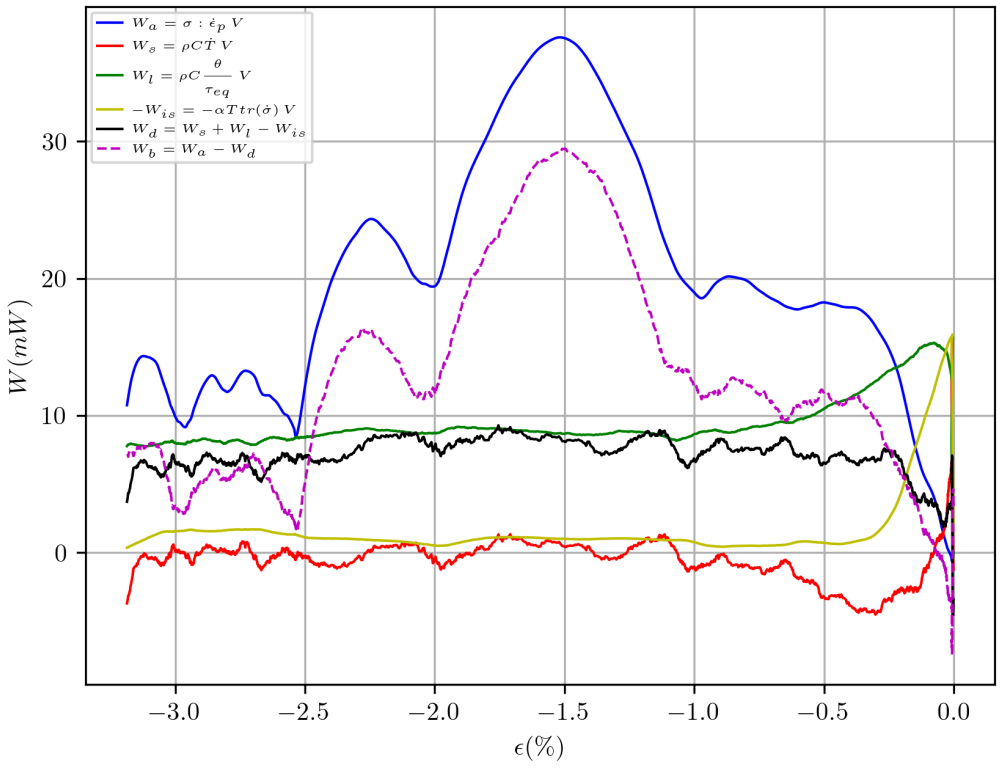

Figure 4.9. Energy terms for cycle 1 compression.

Figure 4.9 shows the variation of energy terms during the loading state 0-1 (cycle 1 compression). The highest amplitude signal in this loading is imposed energy (W_a) due to plastic works. After the elastic region (over twin plateau, around -1.5% axial strain) it increases up to about 40 mW. Then, it decreases gradually to 10 mW at the end of the experiment. During the loading, generated heat dissipates easily due to the high thermal conductivity of magnesium and temperature of the sample increase in mK level. So W_s term fluctuates around 0 after the elastic deformation. It increases up to 15 mW at the elastic region. W_l increases to 15 mW at the end of the elastic deformation and then declines to 10 mW and gets stable. W_{is} reaches its maximum value at elastic deformation, then fluctuates around 0. After all, elastic coupling is not expected in the twinning regime where stress remains largely constant.

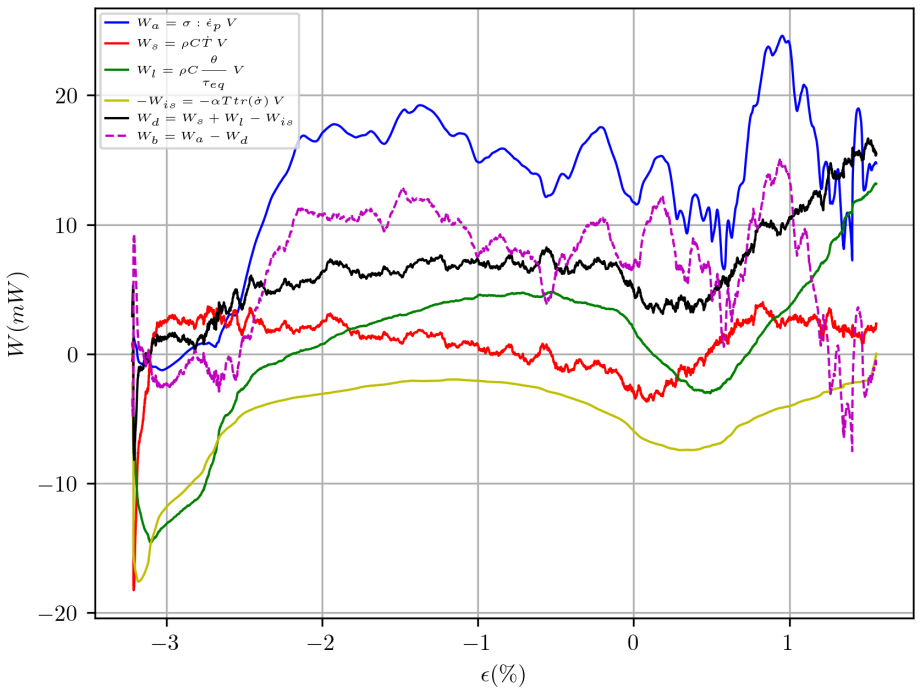

Figure 4.10. Energy terms for cycle 1 tension.

Figure 4.10 shows the variation of energy terms during the loading state 0-1 (cycle 1 tension). Like compression, W_a is the highest amplitude signal and W_s fluctuates around 0 due to low-temperature increase. The important finding in this graph is

that trend changes over W_a at -0.5% strain. Previously, after the detwinning, the existence of the second elastic region (temperature drop in Figure 4.7 after 20 s) is mentioned. The decreasing trend in the total imposed plastic work curve validates the elastic deformation after detwinning. Also, the rise in total imposed plastic work (W_a) trend after 0.5% strain in Figure 4.10, indicates the increase in slip-plasticity activities.

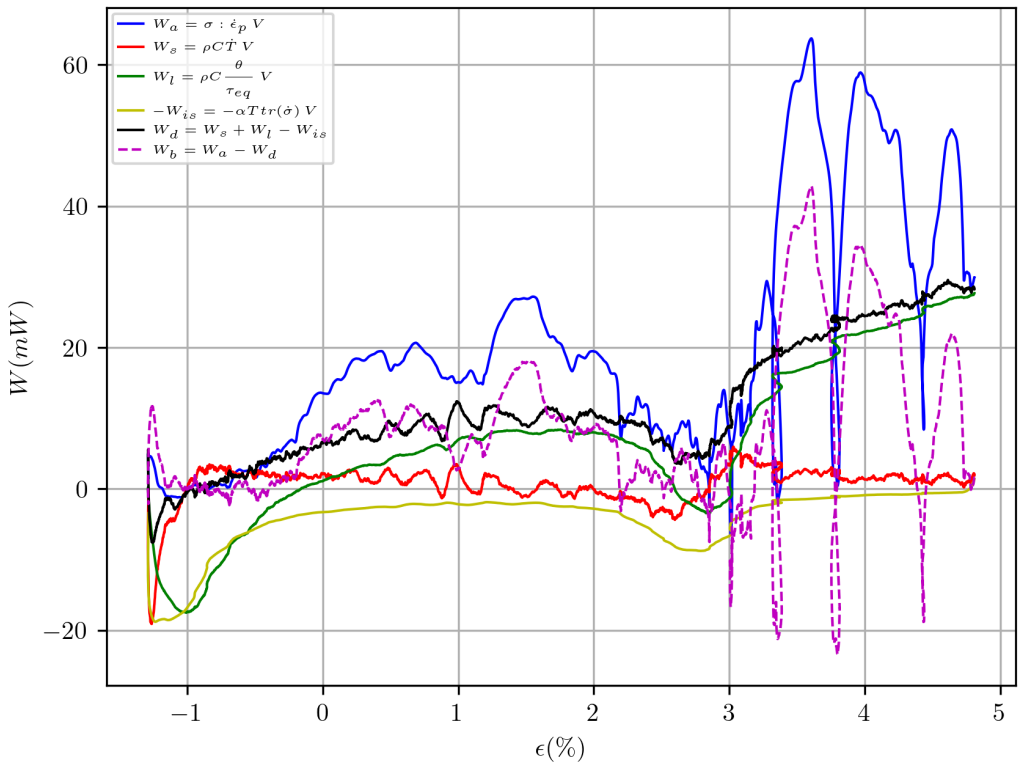

Figure 4.11. Energy terms for cycle 4 tension.

Figure 4.11 shows the variation of energy terms during cycle 4 tension (loading state 7-8). The duration of cycle 4 tension loading is relatively long (can be seen in 4.1) compared to other loadings. The duration of the loading state is specified higher than other rest of the loadings. The sample is loaded relatively higher than other cycles to observe the effect of slip plasticity on energy terms. It is clearly seen that the amplitude of plastic work in slip-dominated plasticity region is twofold higher than detwinning-dominated plasticity region.

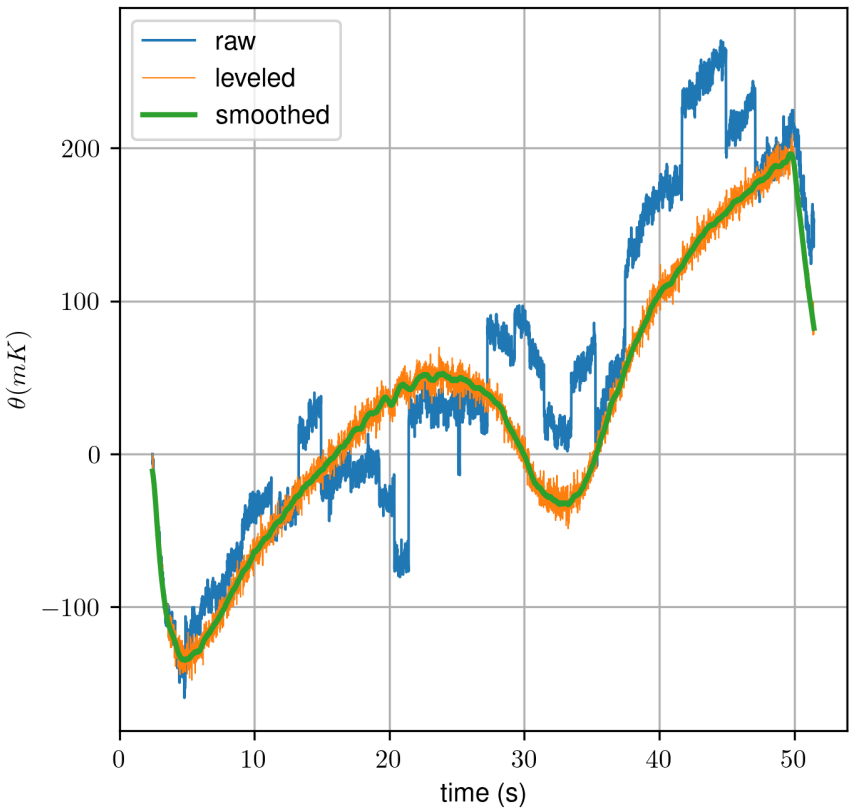

Figure 4.12. Overall temperature profile in cycle 4 tension.

Figure 4.12 shows the temperature difference profile between deformed and reference ROIs (shown in Figure 4.4a) in cycle 4 tension. Figure 4.12 shows similar trends with cycle 1 tension test (shown in Figure 4.7). The sample is loaded in cyclic 4 tension relatively higher than each loading state (see Table 4.1) to see thermal response of slip-dominated region explicitly. It is clearly seen that temperature increase continues after second temperature drop (related to second elastic deformation region in tension), and reach higher values compared to other loading.

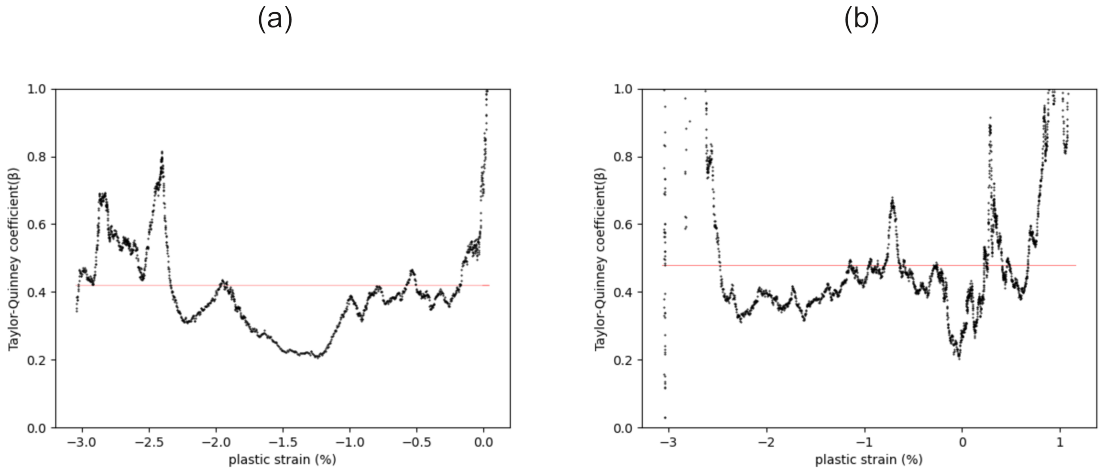

Figure 4.13. Taylor-Quinney coefficient variation during (a) cycle 1 compression (b) cycle 1 tension; red lines correspond to averages.

Another item for the identification of energy sources in cyclic deformation is the Taylor-Quinney examination. The Taylor-Quinney coefficient is an indicator of the amount of plastic work that is dissipated as a heat during deformation. The remaining amount of work is stored in the material. Taylor-Quinney coefficient is not a constant factor and changes during the experiment. There is no study in the literature to reveal the Taylor-Quinney coefficient for magnesium under cyclic loading.

The proportion of each energy budget is calculated for each loading continuously (e.g., see Figure 4.9), so the profile of the Taylor-Quinney coefficient can be calculated with Equation (4.1). Figures 4.13a and b show the variation of the Taylor-Quinney coefficient for cycle 1 compression and tension, respectively. It is clearly shown that (β) fluctuates from 0.8 to 0.2 in tension and compression, but the average value is similar

in both loading (about 0.4-0.5). The average value of the Taylor-Quinney coefficient is lower in compression (0.4) than tension (0.45) for Mg AZ31. Taylor-Quinney coefficients in this thesis are similar to the work closest to our study in the literature [36].

5. DISCUSSION

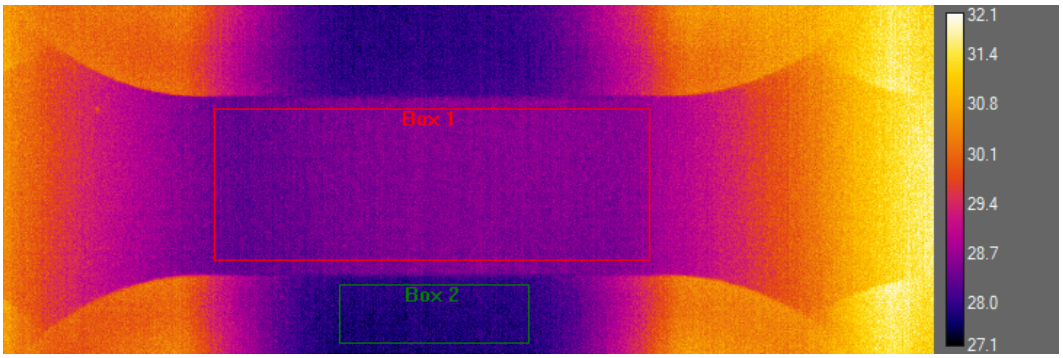

Figure 5.1. Reference (bottom rectangle) and deformed (top rectangle) ROIs on a representative thermal image for titanium specimen.

As previously mentioned, some percentage of plastic work transforms to heat during deformation, and the Taylor-Quinney coefficient represents this ratio. The proportion of dissipated heat (β) is calculated with temperature variation during deformation by IRT. Generally, the temperature of the sample increases continuously under loading. It is demonstrated that (in Figure 4.7) a temperature drop is observed at magnesium in the tension part of the cyclic loading. This is not a common material response for tensile loading. Therefore, the titanium sample is loaded in tension and compression to indicate the temperature profile of magnesium and titanium under the same loading conditions (same displacement rate and duration). Also, this effort emphasizes the uniqueness of magnesium thermal behavior in tension. In this comparison, the absolute temperature change is not targeted; thus, reference metal is not attached to magnesium and titanium. A region that is not affected by loading is selected as a reference to reveal temperature difference trends during the experiment for two materials. ROIs for deformed (box 1 in Figure 5.1) and reference (box 2 in Figure 5.1) material are shown over thermal image of titanium.

Figure 5.2 shows the temperature profile for titanium and magnesium in both compression and tension. It is clearly seen that the thermo-elastic response is the same in both titanium and magnesium. The temperature increase in magnesium reaches

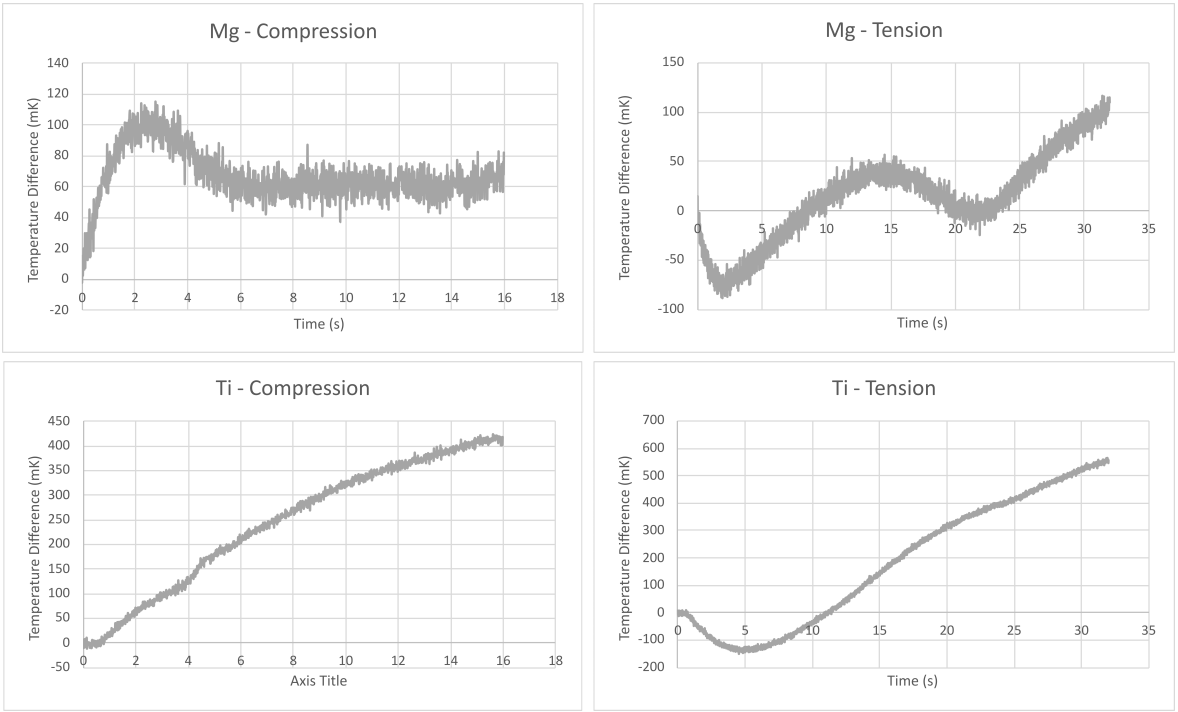

Figure 5.2. Temperature profile comparison between magnesium and titanium both in compression and tension.

its maximum value right after the elastic deformation with 100 mK, temperature rise in titanium reaches its maximum at the final position of the loading with 400 mK for compression. There are four times difference valid between these materials. In tension there are five times difference between magnesium and tension in temperature differences with 100 mK and 500 mK. Also, the major difference between the two materials is the second temperature drop that is seen in the tensile deformation of magnesium. There is no second elastic deformation behavior in titanium contrary to magnesium. Slip plasticity in titanium keeps going after the elastic deformation, and the temperature increase rate rise continuously.

To compare magnesium and titanium in similar conditions, the dimensions of the specimen are kept identical for magnesium and titanium samples. Firstly, the thermal conductivity of pure titanium is relatively small compared to magnesium (14 W/m^2 [43] and 96.4 W/m^2 [44] for commercially pure titanium and Mg AZ31). There is more than five times difference between these materials in thermal conductivity. The measurement

capability of generated heat during deformation depends on the thermal conductivity. When a material is good thermal conductor, heat easily transfers from the deformed region to the undeformed region like the magnesium case.

The other item for discussion is novelties of in situ micro-DIC (Section 4.1) compared to previous work that are conducted in our laboratory. Unlike the work of Kapan et al. [14], which reveals macroscopic shear band patterns on both textures, in situ micro-DIC test (Section 4.1) investigates the intricate nature of twin-driven shear bands with 70 times higher optical resolution. Therefore, interwoven fabric of twin-driven shear bands is observed in detail both rolled and extruded samples. Secondly, high load/time-step resolution and field coverage is employed in area scanning DIC in Section 4.1 compared to previous works in our laboratory. Aydıner and Telemez [12] and Shafaghi et al., [13] utilize the scanning microscopic DIC method to quantify twin-driven shear bands previously. Precisive features of this thesis in regard to previous DIC studies are high load/time-step resolution (0.05-0.1% nominal strain increments over the twin plateau) and extensive field coverage ($\sim 1.5 \times 10^5$ grains) with higher data point ($\sim 10^2$ data points per grain).

6. CONCLUSION

The thermal behavior of magnesium AZ31 is investigated under cyclic loading in this thesis. IRT measurements are conducted to measure the temperature field of the sample. This thesis reveals stored energy during cyclic deformation. The reversal load path allows to investigate detwinning in addition to $\{10\bar{1}2\}(\bar{1}011)$ tensile twin system in terms of thermal behavior. Approximately 50% of the imposed plastic work converts to heat that dissipates from the sample during both compression and tension in cyclic loading.

The temperature profile of the titanium sample is examined both tension and compression in addition to in situ IRT cyclic test (Section 4.2). One major outcome of this comparison is expressing the unique temperature profile of tension loading after compression in magnesium. In contrast to titanium, magnesium shows another elastic deformation after detwinning. There is a temperature drop in this elastic deformation region between detwinning and slip plasticity regions.

Furthermore, the Taylor-Quinney coefficient (β) of magnesium is calculated for both tension and compression in terms of total imposed plastic work and intrinsic dissipation. Taylor-Quinney coefficient is not stable during compression and tension. It fluctuates from 0.2 to 0.8 but the average of these trends converges to 0.4 and 0.5.

As another major branch of this study, strain accommodation characteristics are investigated both rolled and extruded textures with cross-notched samples. With proposed notch configuration is specifically carved along TD twin-driven shear bands successfully guided and overlapped over the intended location. Macroscopically seen shear bands are guided from the corridor of offset notches; meantime, shear bands are overlapped at the middle of the sample.

Extruded sample with the same dimension as the rolled sample is loaded along ED compression as a control experiment. This thesis reveals that transversely isotropic material shows more homogenous strain accommodation in compression compared to severely anisotropic rolled material with this notch configuration which is proposed in this work. Finite element analysis is conducted to support strain accommodation characteristics in control experiment, and this is accomplished successfully.

7. FUTURE WORK

Within the scope of this thesis, spatial temperature signal is tried to find where twinning and detwinning takes place. Spatial resolution for these deformation modes was not observed for some reasons, such as minimal sample dimensions, the high thermal conductivity of the material, the insufficient spatial resolution of IR camera, and insufficient imposed strain rates.

Finite elements analysis is conducted in Abaqus to validate sample dimensions effect over spatial resolution of IRT. A sample whose dimensions are multiplied by 1000 is loaded with same displacement rate as our case in finite element runs. A correlation is observed between the temperature field and plastic strain contour. Therefore, bigger specimens should be designed, and thermal behavior should be examined in a cyclic way to investigate twinning and detwinning.

As presented in Section 4.2, the stress-strain curve of the cyclic experiment shifted to the right due to an unwanted effect of the machine compliance. Therefore, sample is loaded more than each loading state at loading state 7-8 deliberately. In further studies, load should be applied in a way to eliminate machine compliance. Therefore, sample can be loaded in a symmetric way.

REFERENCES

1. Bettles, C. and M. Barnett, *Advances in Wrought Magnesium Alloys: Fundamentals of Processing, Properties and Applications*, Woodhead Publishing, Philadelphia, 2012.

2. Lou, X. Y., M. Li, R. K. Boger, S. R. Agnew and R. H. Wagoner, "Hardening Evolution of AZ31B Mg Sheet", *International Journal of Plasticity*, Vol. 23, No. 1, pp. 44–86, 2007.

3. Agnew, S. R., M. H. Yoo and C. N. Tomé, "Application of Texture Simulation to Understanding Mechanical Behavior of Mg and Solid Solution Alloys Containing Li or Y", *Acta Materialia*, Vol. 49, No. 20, pp. 4277–4289, 2001.

4. Christian, J. W. and S. Mahajan, "Deformation Twinning", *Progress in Materials Science*, Vol. 39, No. 1-2, pp. 1–157, 1995.

5. Chu, F. and D. P. Pope, "Deformation Twinning in Intermetallic Compounds-the Dilemma of Shears vs. Shuffles", *Materials Science and Engineering, A*, Vol. 170, No. 1-2, pp. 39–47, 1993.

6. Brown, D. W., S. R. Agnew, M. A. M. Bourke, T. M. Holden, S. C. Vogel and C. N. Tomé, "Internal Strain and Texture Evolution During Deformation Twinning in Magnesium", *Materials Science and Engineering A*, Vol. 399, No. 1-2, pp. 1–12, 2005.

7. Aydıner, C. C., J. V. Bernier, B. Clausen, U. Lienert, C. N. Tomé and D. W. Brown, "Evolution of Stress in Individual Grains and Twins in a Magnesium Alloy Aggregate", *Physical Review B*, Vol. 80, No. 2, 2009.

8. Wu, L., S. R. Agnew, Y. Ren, D. W. Brown, B. Clausen, G. M. Stoica, H. R. Wenk and P. K. Liaw, "The Effects of Texture and Extension Twinning on the Low-Cycle

Fatigue Behavior of a Rolled Magnesium Alloy, AZ31B", *Materials Science and Engineering A*, Vol. 527, No. 26, pp. 7057–7067, 2010.

9. Ecob, N. and B. Ralph, "The Effect of Grain Size on Deformation Twinning in a Textured Zinc Alloy", *Journal of Materials Science*, Vol. 18, No. 8, pp. 2419–2429, 1983.

10. Barnett, M. R., M. D. Nave and A. Ghaderi, "Yield Point Elongation due to Twinning in a Magnesium alloy", *Acta Materialia*, Vol. 60, No. 4, pp. 1433–1443, 2012.

11. Beyerlein, I. J., L. Capolungo, P. E. Marshall, R. J. McCabe, C. N. Tome and C. Tomé, "Statistical Analyses of Deformation Twinning in Magnesium", *Philosophical Magazine*, Vol. 90, No. 16, pp. 2161–2190, 2010.

12. Aydıner, C. C. and M. A. Telemez, "Multiscale Deformation Heterogeneity in Twinning Magnesium Investigated with In Situ Image Correlation", *International Journal of Plasticity*, Vol. 56, pp. 203–218, 2014.

13. Shafaghi, N., E. Kapan and C. C. Aydıner, "Cyclic Strain Heterogeneity and Damage Formation in Rolled Magnesium Via In Situ Microscopic Image Correlation", *Experimental Mechanics*, Vol. 60, No. 6, pp. 735–751, 2020.

14. Kapan, E., N. Shafaghi, S. Ucar and C. C. Aydıner, "Texture-Dependent Character of Strain Heterogeneity in Magnesium AZ31 Under Reversed Loading", *Materials Science and Engineering A*, Vol. 684, pp. 706–711, 2017.

15. Vidyasagar, A., A. D. Tutcuoglu and D. M. Kochmann, "Deformation Patterning in Finite-Strain Crystal Plasticity by Spectral Homogenization with Application to Magnesium", *Computer Methods in Applied Mechanics and Engineering*, Vol. 335, pp. 584–609, 2018.

16. Cheng, J. and S. Ghosh, "Crystal Plasticity Finite Element Modeling of Discrete

Twin Evolution in Polycrystalline Magnesium", *Journal of the Mechanics and Physics of Solids*, Vol. 99, pp. 512–538, 2017.

17. Cheng, J., J. Shen, R. K. Mishra and S. Ghosh, "Discrete Twin Evolution in Mg Alloys Using a Novel Crystal Plasticity Finite Element Model", *Acta Materialia*, Vol. 149, pp. 142–153, 2018.

18. Mareau, C. and M. R. Daymond, "Micromechanical Modelling of Twinning in Polycrystalline Materials: Application to Magnesium", *International Journal of Plasticity*, Vol. 85, pp. 156–171, 2016.

19. Proust, G., C. N. Tomé, A. Jain and S. R. Agnew, "Modeling the Effect ofTwinning and Detwinning During Strain-Path Changes of Magnesium Alloy AZ31", *International Journal of Plasticity*, Vol. 25, No. 5, pp. 861–880, 2009.

20. Üçel, I. B., E. Kapan, O. Türkoğlu and C. C. Aydıner, "In Situ Investigation of Strain Heterogeneity and Microstructural ShearBands in Rolled Magnesium AZ31", *International Journal of Plasticity*, Vol. 118, pp. 233–251, 2019.

21. Zubelewicz, A., "Century-Long Taylor-Quinney Interpretation of Plasticity-Induced Heating Reexamined", *Scientific Reports*, Vol. 9, No. 1, pp. 1–7, 2019.

22. Rittel, D., A. A. Kidane, M. Alkhader, A. Venkert, P. Landau and G. Ravichandran, "On the Dynamically Stored Energy of Cold Work in Pure Single Crystal and Polycrystalline Copper", *Acta Materialia*, Vol. 60, No. 9, pp. 3719–3728, 2012.

23. Rittel, D., L. Zhang and S. Osovski, "The Dependence of the Taylor–Quinney Coefficient on the Dynamic Loading Mode", *Journal of the Mechanics and Physics of Solids*, Vol. 107, pp. 96–114, 2017.

24. Erman, S. C., L. Stainier and C. C. Aydıner, "Guiding Severely Anisotropic Twinning Bands in Magnesium: An In Situ Investigation by Full-Field Microscopic Image Correlation", *Materials Today Communications*, Vol. 35, p. 106203, 2023.

25. Chang, Y. and D. M. Kochmann, "A Variational Constitutive Model for Slip-Twinning Interactions in Hcp Metals: Application to Single- and Polycrystalline Magnesium", *International Journal of Plasticity*, Vol. 73, pp. 39–61, 2015.

26. Wu, Z., M. F. Francis and W. A. Curtin, "Magnesium Interatomic Potential for Simulating Plasticity and Fracture Phenomena", *Modelling and Simulation in Materials Science and Engineering*, Vol. 23, No. 1, pp. 1–19, 2015.

27. Yoo, M. H. and J. K. Lee, "Deformation Twinning in H.C.P. Metals and Alloys", *Philosophical Magazine A*, Vol. 63, No. 5, pp. 987–1000, 1991.

28. Hosford, W. F., *Mechanical Behavior of Materials*, Cambridge University Press, Cambridge, 2009.

29. Anten, K. and B. Scholtes, "Formation of Macroscopic Twin Bands and Inhomogeneous Deformation During Cyclic Tension-Compression Loading of the Mg-Wrought Alloy AZ31", *Materials Science and Engineering A*, Vol. 746, pp. 217–228, 2019.

30. Bagavathiappan, S., B. B. Lahiri, T. Saravanan, J. Philip and T. Jayakumar, "Infrared Thermography for Condition Monitoring - A Review", *Infrared Physics and Technology*, Vol. 60, pp. 35–55, 2013.

31. Pandey, K. N. and S. Chand, "Deformation Based Temperature Rise: A Review", *International Journal of Pressure Vessels and Piping*, Vol. 80, No. 10, pp. 673–687, 2003.

32. Kapoor, R. and S. Nemat-Nasser, "Determination of Temperature Rise During High Strain Rate Deformation", *Mechanics of Materials*, Vol. 27, No. 1, pp. 1–12, 1998.

33. Hartley, K. A., J. Duffy and R. H. Hawley, "Measurement of the Temperature Profile Durıng Shear Band Formation in Steels Deforming at High Strain Rates", *Journal of the Mechanics and Physics of Solids*, Vol. 35, No. 3, pp. 283–301, 1987.

34. Eisenlohr, A., I. Gutierrez-Urrutia and D. Raabe, "Adiabatic Temperature Increase Associated with Deformation Twinning and Dislocation Plasticity", *Acta Materialia*, Vol. 60, No. 9, pp. 3994–4004, 2012.

35. Ghosh, D., O. T. Kingstedt and G. Ravichandran, "Plastic Work to Heat Conversion During High-Strain Rate Deformation of Mg and Mg Alloy", *Metallurgical and Materials Transactions A: Physical Metallurgy and Materials Science*, Vol. 48, No. 1, pp. 14–19, 2017.

36. Kingstedt, O. T. and J. T. Lloyd, "On the Conversion of Plastic Work to Heat in Mg Alloy AZ31B for Dislocation Slip and Twinning Deformation", *Mechanics of Materials*, Vol. 134, pp. 176–184, 2019.

37. Yilmaz, A., "The Portevin-Le Chatelier Effect: A Review of Experimental Findings", *Science and Technology of Advanced Materials*, Vol. 12, No. 6, 2011.

38. Ait-Amokhtar, H., C. Fressengeas and S. Boudrahem, "The Dynamics of Portevin-Le Chatelier Bands in an Al-Mg Alloy From Infrared Thermography", *Materials Science and Engineering A*, Vol. 488, No. 1-2, pp. 540–546, 2008.

39. Bodelot, L., E. Charkaluk, L. Sabatier and P. Dufrénoy, "Experimental Study of Heterogeneities in Strain and Temperature Fields at the Microstructural Level of Polycrystalline Metals Through Fully-Coupled Full-Field Measurements by Digital Image Correlation and Infrared Thermography", *Mechanics of Materials*, Vol. 43, No. 11, pp. 654–670, 2011.

40. Doudard, C., S. Calloch, F. Hild and S. Roux, "Identification of Heat Source Fields from Infrared Thermography: Determination of 'Self-Heating' in a Dual-Phase Steel by Using a Dog Bone Sample", *Mechanics of Materials*, Vol. 42, No. 1, pp. 55–62, 2010.

41. Chrysochoos, A. and F. Belmahjoub, "Thermographic Analysis of Thermomechani-

cal Couplings", *Archives of Mechanics*, Vol. 44, No. 1, pp. 55–68, 1992.

42. Bachmann, F., R. Hielscher and H. Schaeben, "Texture Analysis with MTEX – Free and Open Source Software Toolbox", *Solid State Phenomena*, Vol. 160, pp. 63–68, 2010.

43. Ashby, M. F., *Materials and the Environment: Eco-Informed Material Choice*, Butterworth-Heinemann, Oxford, 2009.

44. Li, S., X. Yang, J. Hou and W. Du, "A Review on Thermal Conductivity of Magnesium and Its Alloys", *Journal of Magnesium and Alloys*, Vol. 8, No. 1, pp. 78–90, 2020.

45. Özdür, N. A., I. B. Üçel, J. Yang and C. C. Aydıner, "Residual Intensity as a Morphological Identifier of Twinning Fields in Microscopic Image Correlation", *Experimental Mechanics*, Vol. 61, No. 3, pp. 499–514, 2021.